J. Fluid Mech. (2007), *vol.* 588, *pp.* 189–215.
doi:10.1017/S0022112007007446 Printed in the United Kingdom

Instability of optimal non-axisymmetric base-flow deviations in pipe Poiseuille flow

GUY BEN-DOV† AND JACOB COHEN

Faculty of Aerospace Engineering, Technion – Israel Institute of Technology, Haifa 32000, Israel
aerycyc@aerodyne.technion.ac.il

(Received 12 November 2006 and in revised form 22 May 2007)

The stability of pipe flow when mildly deviating from the developed Poiseuille profile by a non-axisymmetric azimuthally periodic distortion is examined. The motivation for this is to consider deviations, the origin of which may be attributed to small-amplitude disturbances having sinusoidal periodicity along the azimuthal coordinate, which are known to be the ones most amplified by the transient growth linear mechanism. A mathematical technique for finding the minimum energy density of azimuthally periodic deviations triggering exponential instability is presented. The results show that owing to bifurcations multiple solutions of optimal deviations exist. As the Reynolds number is increased additional bifurcations appear and create more distinct solutions. The different solutions correspond to different radial distributions of the deviations, and at Reynolds numbers of about 2000 they are distributed over less than a half of the pipe radius. It is found that the dependence of the optimal deviation velocity leading to instability on the Reynolds number Re is approximately $20/Re$. A comparison to axisymmetric base-flow deviations shows that the minimum energy required for an azimuthally periodic deviation to trigger instability is almost twice that for the axisymmetric flow. However, azimuthally periodic deviations, which are shown to have a streaky pattern, may have a role in the self-sustaining process. They may be formed as a result of a transient growth amplification of initial streamwise rolls and can produce, via self-interactions between the resulting growing waves, patterns of streamwise rolls as well.

1. Introduction

The phenomenon of transition from laminar to turbulent flow in a pipe has been explored in many studies since the first known experiments by Reynolds (1883). In his experiments Reynolds observed that transition depends on a dimensionless quantity $Re = 2\bar{W}R/\nu$ (referred to since then as the Reynolds number), based on the average (bulk) axial velocity $\bar{W}$, the pipe radius R and the kinematic viscosity ν. In an extensive study, Reynolds found that in various tubes having different diameters the steady motion changed into an unsteady flow, in which eddies could be observed, for Re above approximately 2000. However, when disturbances were carefully avoided this transition could be delayed to much higher Re of 12000 to 14000; when the pipe is smooth and inlet conditions are carefully controlled transition to turbulence can be delayed to much higher values of the Reynolds number (in an experiment by Pfeniger 1961, laminar flow has been sustained for Reynolds numbers up to 10^5).

† Present address: University of Illinois at Urbana-Champaign, 1206 West Green St, Urbana, IL 61801, USA; guyb@uiuc.edu.

According to linear stability analysis, a developed pipe flow is known to be stable to any kind of infinitesimal disturbance for all Reynolds numbers. This result has been shown numerically to hold for Reynolds numbers up to 10^6–10^7 for a wide range of axial and azimuthal wavenumbers (Lessen, Sadler & Liu 1968; Salwen, Cotton & Grosch 1980; Meseguer & Trefethen 2003). In many experiments performed during the past decades transition to turbulence has been observed at Reynolds numbers $1800 < Re < Re_u$, where the upper bound value Re_u depends on the magnitude of the disturbance amplitude, naturally initiated or artificially introduced into the flow (e.g. see Wygnanski & Champagne 1973; Wygnanski, Sokolov & Friedman 1975; Rubin, Wygnanski & Haritonidis 1980; Darbyshire & Mullin 1995; Eliahou, Tumin & Wygnanski 1998; Han, Tumin & Wygnanski 2000; Hof, Juel & Mullin 2003).

Since the developed flow in a pipe has been shown to be linearly stable, exploring weakly nonlinear instabilities has been attempted in a wide variety of studies. For example, Davey & Nguyen (1971) and later Itoh (1977) considered finite-amplitude expansions for axisymmetric disturbances which were assumed to be valid in the $Re \to \infty$ limit. Numerical results obtained by Orszag & Patera (1983) showed the existence of non-axisymmetric secondary instabilities, where the primary state consisted of axisymmetric finite-amplitude waves. Smith & Bodonyi (1982) applied a nonlinear critical layer theory at asymptotically large Reynolds numbers and found neutral, finite-amplitude disturbances, having a helical structure.

Pipe flow is one example of wall-bounded shear flows in which transition may occur for Re lower than the critical value predicted by linear stability theory. Other known examples are plane Couette flow, which has been shown to be linearly stable for any Reynolds number (Romanov 1973), and plane Poiseuille flow, which has been found to be linearly unstable only for Re greater than approximately 5800 (Thomas 1953). In both flows transition has been observed at subcritical Reynolds numbers (e.g. see the subcritical transition experiments by Tillmark & Alfredsson 1992 for plane Couette flow and by Patel & Head 1969 for plane Poiseuille flow).

A possible subcritical transition scenario is due to the transient growth mechanism (see the review paper by Reshotko 2001 and the book by Schmid & Henningson 2001). Accordingly, small finite initial disturbances may initially be significantly amplified and trigger nonlinear instabilities, before their decay due to viscous effects. For plane Poiseuille flow Gustavsson (1991) found that the most amplified disturbances are streamwise-independent three-dimensional structures. Butler & Farrell (1992) have applied an optimization procedure for plane Couette and plane Poiseuille flows to yield the most amplified initial disturbances. They found that the most transiently amplified disturbances have the structure of streamwise vortices, independent of the streamwise direction. Optimal transient growth analysis in pipe flows has been carried out by Bergström (1993) and by Schmid & Henningson (1994) for temporally growing disturbances, and by Reshotko & Tumin (2001) for spatial disturbances. It has been shown in the first two studies above that the most amplified initial disturbances have a helical structure and are independent of the streamwise direction. The last work has shown similar results; however, in this case the most amplified disturbances have been found to be stationary. Schmid & Henningson (1994) have also shown that the most transiently amplified initial disturbances have the structure of two counter-rotating vortices in the pipe cross-section.

Ben-Dov, Levinski & Cohen (2003) have demonstrated that in a fully developed pipe flow the time and distance, at which the maximum energy amplification of an initial disturbance is achieved, are well-predicted analytically by considering only the pair of least-stable modes. Furthermore, the dependence of the maximum energy amplification on the Reynolds number matches previous numerical results which were

based on the analysis of many modes. In the temporal case the predicted amplification factor agrees well with these numerical results. Moreover, for both temporal and spatial analysis the initial structure consisting of two counter-rotating vortices has been shown to be obtained from the two least-stable modes. The induced wall-normal velocity of the counter-rotating streamwise vortices produces low- and high-speed streamwise regions, which are commonly termed 'streaks' (e.g. see the experiments by Elofsson & Alfredsson 1998 and by Svizher & Cohen 2006 for plane Poiseuille flow).

The transient growth mechanism, considered in the above-mentioned studies, is purely linear and is assumed to be followed by a nonlinear stage, leading to transition. This nonlinear stage has been addressed by Zikanov (1996) for the case of pipe Poiseuille flow. In that study finite-amplitude disturbances have been introduced into the flow, and their evolution was traced in two steps. In the first step, using direct numerical simulations, the initial flow-field included optimal helical initial streamwise vortices, like the ones found by Bergström (1993) and by Schmid & Henningson (1994) based on linear theory. The pipe Poiseuille base flow has been thus initially modulated and for sufficiently strong vortices, streaks appeared after some transient time. In the second step, the amplified streaks have been used as part of the base flow for linear stability analysis with respect to secondary disturbances. The analysis revealed that this modified base flow is unstable with respect to certain three-dimensional modes. However, the maximum amplification of the modulated base flow and the time at which it is attained are at least one order of magnitude less than the corresponding values predicted by the linear transient growth theory. In a complementary numerical study by Meseguer (2003), the nonlinear evolution of the infinitesimal secondary three-dimensional modes has been followed, using the same base flow, i.e. pipe Poiseuille flow together with finite-amplitude streamwise independent perturbations. It has been shown that throughout this nonlinear stage certain secondary instabilities do not decay.

Similar transition scenarios have also been examined in plane Couette and plane Poiseuille flows (e.g. see Gustavsson 1991; Butler & Farrell 1992; Reddy & Henningson 1993; Henningson, Lundbladh & Johansson 1993). Correspondingly, the transition consists of two stages. The first stage begins with the formation of streamwise vortices (approximately aligned with the basic laminar flow) and the subsequent formation of streamwise streaks of relatively low and high velocity in the azimuthal (spanwise)-direction. This is a linear stage, governed by the transient growth (algebraic) mechanism. The second stage is the final evolution of a secondary instability of oblique modes (i.e. a perturbation which is streamwise dependent). By examining the linearized wall-normal vorticity equation asymptotically for $Re \to \infty$, it is evident that the transient growth amplification (in the first stage) of streamwise modes, having infinitely long streamwise wavelength ($\sim Re$), is proportional to Re over a time scale of $O(Re)$. In other words, an initial wall-normal velocity perturbation with an amplitude ε will result in a transient growth amplification of the wall-normal vorticity η with magnitude of $O(\varepsilon Re)$ (see the study by Chapman 2002). Hence, for infinitesimal perturbations, the maximum transient growth amplification will not be achieved until the perturbation has travelled a distance of $O(Re)$.

Experimentally, however, typical subcritical transition requires much shorter downstream distances (less than $\sim$50 pipe diameters or channel widths, e.g. see Darbyshire & Mullin 1995 or Elofsson & Alfredsson 1998). The long distance (or time) of order Re required for transient growth of infinitesimal perturbations can be significantly shortened by increasing the initial amplitude ε. The wall-normal vorticity equation shows that $\eta \sim \varepsilon Re(t/Re)$, where t denotes the non-dimensional time (normalized by the pipe centreline axial velocity and the pipe radius). When

$t \sim Re$, a small ε ($\sim 1/Re$) can give an $O(1)$ amplification in η. However, the same effect can be achieved for much shorter times by increasing ε equivalently. This scenario was recently used by Philip, Svizher & Cohen (2007) to experimentally confirm the two-stage scaling law of subcritical transition in plane Poiseuille flow, asymptotically derived by Chapman (2002). Moreover, if the initial perturbation is not infinitesimally small, a different approach may also explain the subcritical transition over a relatively short distance. As pointed out by several investigators (e.g. Biau & Bottaro 2004), an exponential growth of one (or more) mode(s) can still exist in nominally subcritical conditions when the mean flow is mildly distorted with respect to the canonical base flow profile. Biau & Bottaro (2004) suggested that such modifications in a base flow can arise in laboratory experiments when operating in less-than-perfect conditions, i.e. under the influence of various forcing terms such as wall roughness, inflow disturbances, pressure gradient fluctuations, vibrations, etc.

The concept of superimposing deviations on a linearly stable base flow has been introduced by Gill (1965) for viscous shear flows and later by Lerner & Knobloch (1988) for an inviscid free shear flow. Bottaro, Corbett & Luchini (2003) presented a variational method to optimize the deviations in parallel shear flows, in order to find the lowest amplitude deviations resulting in an unstable modified base-flow. Bottaro *et al.* (2003) and Biau & Bottaro (2004) have analysed the temporal and spatial instabilities, respectively, of two-dimensional optimal deviations added to plane Couette and plane Poiseuille flows. In the latter study the optimal deviations have been termed 'minimal defects'. Gavarini, Bottaro & Nieuwstadt (2004) have used the same method to investigate the spatial instability of pipe flows to optimal axisymmetric deviations. They have found that unstable modes exist for a very small deviation magnitude at Reynolds numbers in the range $Re = 1000$–4000, and that the instability is essentially governed by an inviscid mechanism (inflection point instability). More recently, Ben-Dov & Cohen (2007) employed the mathematical method introduced by Gavarini *et al.* (2004) and through a careful examination of the nonlinear features of this problem revealed a 'critical Reynolds number' of ~ 2000 associated with the bifurcation between two deviation solutions. Below this Re the minimal deviation is concentrated next to the pipe wall whereas above it the minimal deviation is around the centre of the pipe. The associated unstable waves of the latter have wavelengths and time scales which are respectively about 2 times and 3.5 times shorter than those of the former. As both the length and time scales of any possible unstable wave solution must be much shorter than the axial length and time scales of the deviation, these characteristics may supply an explanation for the preference of the solution, i.e. only if the deviation persists over a sufficiently long time and spatial extent compared to the respective scales of the unstable waves can the latter grow and initiate transition.

In the present work we examine the stability of the base-flow profile when it is mildly deviated from the Poiseuille profile by a non-axisymmetric azimuthally periodic distortion. The motivation for this is to consider deviations, the origin of which may be attributed to the transient growth of relatively small disturbances. In other words, as the structure of the optimal transiently growing initial disturbance varies along the azimuthal coordinate θ as $\cos(\theta)$ (e.g. see Bergström 1993), the resulting deviations are expected to vary periodically with θ as well. Their radial distribution is optimized to find the lowest amplitude required to trigger instability. Unlike the wake-like instability described by Waleffe (1997), and considered by Wedin & Kerswell (2004) for pipe flows, in the present case the instability mechanism is based on an inflection in the radial direction rather than in the azimuthal (or spanwise in a channel flow)

coordinate. It is reasonable that at high Reynolds numbers weak streaky structures (relative to the mean flow) may become unstable, i.e. at high Reynolds numbers the streaks may not have to reach the order of magnitude of the mean flow in order to trigger instability.

In the following we find optimal deviations to the pipe Poiseuille flow. Unlike previous studies mentioned above, in which two-dimensional (axisymmetric) deviations have been considered, in the present case the deviations are three-dimensional. They are independent of the streamwise direction but vary along the azimuthal direction. Thus, they represent a streaky structure in which the radial distribution of the axial velocity is optimized to have a minimal amplitude, required for the modified base flow to become linearly unstable. Section 2 presents the governing equations for a base flow consisting of the Poiseuille pipe flow modified by an azimuthally periodic deviation. In § 3 the optimization method for azimuthally periodic deviations is developed. Section 4 presents the results, including a brief overview of axisymmetric deviations, mainly for comparison with the azimuthally periodic deviation results presented later, and an analysis of the flow induced by the unstable waves triggered by the azimuthally periodic deviations. Section 5 is a discussion on the transition scenarios emerging from the results, and finally § 6 presents the concluding remarks.

2. Governing equations for azimuthally periodic base-flow deviations

A cylindrical coordinate system (r, θ, z) is introduced, where r, θ and z denote the radial, azimuthal, and axial directions, respectively. The governing equations for linear disturbances are the linearized Navier–Stokes equations, which are solved for incompressible flow in non-dimensional form, using the centreline base-flow velocity W_0 ($W_0 = 2\bar{W}$) and the pipe radius R as characteristic scales. The axial base-flow velocity is the sum of the known parabolic profile $W_p = 1 - r^2$ and a non-axisymmetric deviation which is periodic in θ, independent of z and having an amplitude $W_d(r)$. In non-dimensional form it is

$$W(r, \theta) = W_p(r) + W_d(r)\cos(\theta). \tag{2.1}$$

Linearizing the Navier–Stokes equations around the laminar solution W yields

$$\frac{1}{r}\frac{\partial(ru)}{\partial r} + \frac{1}{r}\frac{\partial v}{\partial \theta} + \frac{\partial w}{\partial z} = 0, \tag{2.2a}$$

$$\frac{\partial u}{\partial t} + W\frac{\partial u}{\partial z} = -\frac{\partial p}{\partial r} + \frac{1}{Re}\left(\nabla^2 u - \frac{u}{r^2} - \frac{2}{r^2}\frac{\partial v}{\partial \theta}\right), \tag{2.2b}$$

$$\frac{\partial v}{\partial t} + W\frac{\partial v}{\partial z} = -\frac{1}{r}\frac{\partial p}{\partial \theta} + \frac{1}{Re}\left(\nabla^2 v - \frac{v}{r^2} + \frac{2}{r^2}\frac{\partial u}{\partial \theta}\right), \tag{2.2c}$$

$$\frac{\partial w}{\partial t} + W\frac{\partial w}{\partial z} + \left(u\frac{\partial}{\partial r} + \frac{v}{r}\frac{\partial}{\partial \theta}\right)W = -\frac{\partial p}{\partial z} + \frac{1}{Re}\nabla^2 w, \tag{2.2d}$$

where

$$\nabla^2 = \frac{1}{r}\frac{\partial}{\partial r}\left(r\frac{\partial}{\partial r}\right) + \frac{1}{r^2}\frac{\partial^2}{\partial \theta^2} + \frac{\partial^2}{\partial z^2},$$

u, v and w are the disturbance velocity components in the r-, θ- and z-directions, respectively, p is the disturbance pressure, and $Re = W_0 R/\nu$ is the Reynolds number where ν denotes the kinematic viscosity.

The coefficients in (2.2) depend on r and are periodic in θ. According to Floquet's theorem the solution can be written as an infinite series of the form

$$\{u, v, w, p\} = \mathrm{e}^{\mathrm{i}(\alpha z-\omega t)} \sum_{n=-\infty}^{\infty} \{u_n(r), v_n(r), w_n(r), p_n(r)\}\mathrm{e}^{\mathrm{i}n\theta}, \tag{2.3}$$

where α is the streamwise wavenumber and ω is the frequency. Substituting (2.3) into (2.2) yields the following set of ordinary equations:

$$(\boldsymbol{M}_n - \mathrm{i}\omega\boldsymbol{D})\boldsymbol{a}_n = -\boldsymbol{L}_1\boldsymbol{a}_{n-1} - \boldsymbol{L}_2\boldsymbol{a}_{n+1}, \tag{2.4}$$

where

$$\boldsymbol{a}_n = \{u_n, v_n, w_n, p_n\}^T, \qquad \boldsymbol{D} = \begin{pmatrix} 0 & 0 & 0 & 0 \\ 1 & 0 & 0 & 0 \\ 0 & 1 & 0 & 0 \\ 0 & 0 & 1 & 0 \end{pmatrix}, \qquad \boldsymbol{M}_n = \sum_{k=0}^{2} \boldsymbol{\mu}_{k,n} \frac{d^k}{dr^k},$$

$$\boldsymbol{\mu}_{2,n} = -\frac{1}{Re}\boldsymbol{D}, \qquad \boldsymbol{\mu}_{1,n} = \begin{pmatrix} 1 & 0 & 0 & 0 \\ -1/(r\,Re) & 0 & 0 & 1 \\ 0 & -1/(r\,Re) & 0 & 0 \\ 0 & 0 & -1/(r\,Re) & 0 \end{pmatrix}, \tag{2.5}$$

$$\boldsymbol{\mu}_{0,n} = \begin{pmatrix} \dfrac{1}{r} & \dfrac{\mathrm{i}n}{r} & \mathrm{i}\alpha & 0 \\ \mathrm{i}\alpha W_p + \dfrac{1}{Re}\left(\dfrac{n^2+1}{r^2} + \alpha^2\right) & \dfrac{2\mathrm{i}n}{r^2 Re} & 0 & 0 \\ -\dfrac{2\mathrm{i}n}{r^2 Re} & \mathrm{i}\alpha W_p + \dfrac{1}{Re}\left(\dfrac{n^2+1}{r^2} + \alpha^2\right) & 0 & \dfrac{\mathrm{i}n}{r} \\ W_p' & 0 & \mathrm{i}\alpha W_p + \dfrac{1}{Re}\left(\dfrac{n^2}{r^2} + \alpha^2\right) & \mathrm{i}\alpha \end{pmatrix}.$$

The superscript T denotes the transpose operation and the prime indicates the derivative with respect to the radial coordinate. The expressions for the two terms on the right-hand side of (2.4) are

$$\boldsymbol{L}_{1,2} = \frac{1}{2}\begin{pmatrix} 0 & 0 & 0 & 0 \\ \mathrm{i}\alpha W_d & 0 & 0 & 0 \\ 0 & \mathrm{i}\alpha W_d & 0 & 0 \\ W_d' & \pm(\mathrm{i}/r)W_d & \mathrm{i}\alpha W_d & 0 \end{pmatrix}, \tag{2.6}$$

where the subscripts 1 and 2 correspond to the plus and minus signs inside the matrix, respectively. When $W_d = 0$ the right-hand side of (2.4) is set to zero and the system is reduced to the eigenvalue problem for pipe Poiseuille flow for a given n, which then represents the azimuthal wavenumber. When the right-hand side of (2.4) exists, the eigenvalue problem associated with a given function $W_d(r)$ consists of an infinite number of coupled sets, corresponding to the terms of the series (2.3). The boundary conditions on the centreline ($r = 0$) for each component of the vector $\boldsymbol{a}_n$ are (Batchelor & Gill 1962)

$$\left.\begin{array}{lll} u_n, v_n = 0, \quad w_n \text{ finite} & \text{for} & n = 0, \\ u_n \pm \mathrm{i}v_n = 0, \quad 2\mathrm{d}u_n/\mathrm{d}r \pm \mathrm{i}\mathrm{d}v_n/\mathrm{d}r = 0, \quad w_n = 0 & \text{for} & n = \pm 1, \\ u_n, v_n, w_n = 0 & \text{for} & |n| > 1. \end{array}\right\} \tag{2.7}$$

The no-slip and no-penetration conditions on the pipe wall ($r=1$) imply $u_n=v_n=w_n=0$.

Assuming convergence of the series (2.3) for a finite number of terms ($-N\leqslant n\leqslant N$, where N is an integer number), the system (2.4) consists of $2N+1$ coupled sets of equations. However, this system possesses a symmetry property, $\{u_n, v_n, w_n, p_n\}=\{u_{-n}, -v_{-n}, w_{-n}, p_{-n}\}$, such that only $N+1$ coupled sets have to be considered. We begin with the solution consisting of $|n|\leqslant 2$. For this case there are three sets of equations, which for the temporal analysis result in an eigenvalue problem for the complex frequency ω. In compact notation the resulting sets of equations are

$$\mathrm{i}\omega \boldsymbol{D}\boldsymbol{a}_0 = \boldsymbol{M}_0\boldsymbol{a}_0 + \boldsymbol{L}_0\boldsymbol{a}_1, \tag{2.8a}$$

$$\mathrm{i}\omega \boldsymbol{D}\boldsymbol{a}_1 = \boldsymbol{M}_1\boldsymbol{a}_1 + \boldsymbol{L}_1\boldsymbol{a}_0 + \boldsymbol{L}_2\boldsymbol{a}_2, \tag{2.8b}$$

$$\mathrm{i}\omega \boldsymbol{D}\boldsymbol{a}_2 = \boldsymbol{M}_2\boldsymbol{a}_2 + \boldsymbol{L}_1\boldsymbol{a}_1, \tag{2.8c}$$

where

$$\boldsymbol{L}_0 = \begin{pmatrix} 0 & 0 & 0 & 0 \\ \mathrm{i}\alpha W_d & 0 & 0 & 0 \\ 0 & 0 & 0 & 0 \\ W_d' & -(\mathrm{i}/r)W_d & \mathrm{i}\alpha W_d & 0 \end{pmatrix}. \tag{2.9}$$

The system (2.8) can be solved for a given azimuthally periodic deviation with the radial distribution $W_d(r)$. For the case $W_d=0$ the three sets of equations are decoupled, and each set yields the known eigenvalue problem of pipe Poiseuille flow for a different azimuthal wavenumber ($n=0, 1, 2$), such that the whole system generates three sets of eigenvalues, one set for each n. As the magnitude of W_d is slightly increased above zero, the eigenvalues deviate (from their values associated with the pure Poiseuille profile) due to the coupling terms. We choose to focus on eigenvalues associated with $n=1$, which for the uncoupled problem (Poiseuille base flow) yield the least-stable eigenvalue. For this choice the set (2.8*b*) is the main eigenvalue system, while the other two sets (2.8*a*) and (2.8*c*) affect the solution only through the deviation W_d. Therefore, it is convenient to substitute the two sets (2.8*a*) and (2.8*c*) into (2.8*b*) to yield the following single set of equations:

$$\mathscr{M}_1\boldsymbol{a}_1 = \boldsymbol{L}_1\mathscr{M}_0^{-1}\boldsymbol{L}_0\boldsymbol{a}_1 + \boldsymbol{L}_2\mathscr{M}_2^{-1}\boldsymbol{L}_1\boldsymbol{a}_1, \tag{2.10}$$

where

$$\mathscr{M}_n \equiv \boldsymbol{M}_n - \mathrm{i}\omega\boldsymbol{D}, \tag{2.11}$$

and the notation $(\ )^{-1}$ indicates inverse operators.

3. Optimizing azimuthally periodic deviations

In the following the variational technique by Gavarini *et al.* (2004), who analysed axisymmetric base-flow deviations, is applied to the case of non-axisymmetric, azimuthally periodic deviations. Accordingly, a variation δW_d in the base-flow profile is introduced, which results in the corresponding variations $\delta\omega$ in the eigenvalue and $\delta\boldsymbol{a}_1$ in the eigenfunctions of the system (2.10). The variational system resulting from (2.8*b*) is

$$\mathrm{i}\delta\omega\boldsymbol{D}\boldsymbol{a}_1 = \mathscr{M}_1\delta\boldsymbol{a}_1 + \delta\boldsymbol{L}_1\boldsymbol{a}_0 + \delta\boldsymbol{L}_2\boldsymbol{a}_2 + \boldsymbol{L}_1\delta\boldsymbol{a}_0 + \boldsymbol{L}_2\delta\boldsymbol{a}_2, \tag{3.1}$$

where the notation $\delta\boldsymbol{L}_j$ ($j=0, 1, 2$) corresponds to the matrices in (2.6) and (2.9), with δW_d and $\delta W_d'$ replacing W_d and W_d', respectively. Similarly, the variational systems

resulting from (2.8a) and (2.8c) are, respectively,

$$\mathscr{M}_0\delta\boldsymbol{a}_0 - \mathrm{i}\delta\omega\boldsymbol{D}\boldsymbol{a}_0 = -\delta\boldsymbol{L}_0\boldsymbol{a}_1 - \boldsymbol{L}_0\delta\boldsymbol{a}_1, \tag{3.2a}$$

$$\mathscr{M}_2\delta\boldsymbol{a}_2 - \mathrm{i}\delta\omega\boldsymbol{D}\boldsymbol{a}_2 = -\delta\boldsymbol{L}_1\boldsymbol{a}_1 - \boldsymbol{L}_1\delta\boldsymbol{a}_1. \tag{3.2b}$$

Substituting (3.2a) and (3.2b) into (3.1) yields the variational system:

$$\begin{aligned}\left[\mathscr{M}_1 - \left(\boldsymbol{L}_1\mathscr{M}_0^{-1}\boldsymbol{L}_0 + L_2\mathscr{M}_2^{-1}\boldsymbol{L}_1\right)\right]\delta\boldsymbol{a}_1 \\ = \mathrm{i}\delta\omega\left(\boldsymbol{D} + \boldsymbol{L}_1\mathscr{M}_0^{-1}\boldsymbol{D}\mathscr{M}_0^{-1}\boldsymbol{L}_0 + \boldsymbol{L}_2\mathscr{M}_2^{-1}\boldsymbol{D}\mathscr{M}_2^{-1}\boldsymbol{L}_1\right)\boldsymbol{a}_1 \\ + \left(\delta\boldsymbol{L}_1\mathscr{M}_0^{-1}\boldsymbol{L}_0 + \delta\boldsymbol{L}_2\mathscr{M}_2^{-1}\boldsymbol{L}_1 + \boldsymbol{L}_1\mathscr{M}_0^{-1}\delta\boldsymbol{L}_0 + \boldsymbol{L}_2\mathscr{M}_2^{-1}\delta\boldsymbol{L}_1\right)\boldsymbol{a}_1.\end{aligned} \tag{3.3}$$

The left-hand side of (3.3) can be eliminated by taking the inner product with the adjoint eigenfunction vector $\boldsymbol{b}_1 = \{u_{1a}, v_{1a}, w_{1a}, p_{1a}\}^T$ as follows. The inner scalar product between two vectors $\boldsymbol{a}$ and $\boldsymbol{b}$ is defined as

$$(\boldsymbol{a}, \boldsymbol{b}) \equiv \int_0^1 r\boldsymbol{b}^\dagger\boldsymbol{a}\mathrm{d}r = \int_0^1 r(u_a^* u + v_a^* v + w_a^* w + p_a^* p)\mathrm{d}r, \tag{3.4}$$

where the superscripts $\dagger$ and $*$ denote the conjugate transpose and the complex conjugate, respectively. The adjoint function $\boldsymbol{b}_1$ is defined by the relation:

$$(\mathscr{L}\boldsymbol{a}_1, \boldsymbol{b}_1) = (\boldsymbol{a}_1, \mathscr{L}_a\boldsymbol{b}_1), \tag{3.5}$$

where $\mathscr{L} \equiv \mathscr{M}_1 - \boldsymbol{L}_1\mathscr{M}_0^{-1}\boldsymbol{L}_0 - \boldsymbol{L}_2\mathscr{M}_2^{-1}\boldsymbol{L}_1$ is the differential operator in the system (2.10), and $\mathscr{L}_a$ denotes its adjoint operator.

By taking the inner product of the system (3.3) with the adjoint eigenfunction $\boldsymbol{b}_1$ we obtain a relation between the variation δW_d in the azimuthally periodic base-flow deviation and the variation in the eigenvalue $\delta\omega$. It should be noted that the resulting relation depends on the radial distribution of the deviation W_d itself (which appears in each of the matrices $\boldsymbol{L}_j$, $j = 0, 1, 2$). For sufficiently small amplitudes of the deviation, the quadratic terms of W_d are negligible compared to the others, and the system (3.3) can be reduced to a more compact one:

$$\mathscr{M}_1\delta\boldsymbol{a}_1 = \mathrm{i}\delta\omega\boldsymbol{D}\boldsymbol{a}_1 + \left(\delta\boldsymbol{L}_1\mathscr{M}_0^{-1}\boldsymbol{L}_0 + \delta\boldsymbol{L}_2\mathscr{M}_2^{-1}\boldsymbol{L}_1 + \boldsymbol{L}_1\mathscr{M}_0^{-1}\delta\boldsymbol{L}_0 + \boldsymbol{L}_2\mathscr{M}_2^{-1}\delta\boldsymbol{L}_1\right)\boldsymbol{a}_1. \tag{3.6}$$

For the reduced system (3.6) the adjoint operator $\mathscr{M}_{1a}$ is simply the adjoint of the linearized Navier–Stokes equations with the pipe Poiseuille base flow and for $n = 1$. With this choice for $\boldsymbol{b}_1$ as the eigenfunction of $\mathscr{M}_{1a}\boldsymbol{b} = 0$, the variation $\delta\omega$ in the eigenvalue can be expressed as

$$\delta\omega = \mathrm{i}\frac{\displaystyle\int_0^1 (\delta W_d\mathscr{G}W_d + W_d\mathscr{G}\delta W_d)\mathrm{d}r}{\displaystyle 4\int_0^1 r\boldsymbol{b}_1^*\boldsymbol{D}\boldsymbol{a}_1\mathrm{d}r}, \tag{3.7}$$

where $\mathscr{G}$ represents a differential operator, resulting from the last terms on the right-hand side of (3.6). For numerical purposes this differential operator should be translated into an algebraic form. The expression for the algebraic form of the operator $\mathscr{G}$ (in terms of differentiation matrices) is presented in appendix A.

Relation (3.7) is now useful for finding the optimal azimuthally periodic deviations for axisymmetric pipe Poiseuille flow. Similarly to the axisymmetric deviation analysis by Gavarini *et al.* (2004), we maximize the disturbances growth rate (imaginary part of the eigenvalues in this case) by satisfying a constraint on the magnitude of the

function W_d, expressed by the norm

$$\int_0^1 r W_d^2 \mathrm{d}r = \epsilon. \tag{3.8}$$

In the following the parameter ϵ is chosen to be small, such that according to (3.8) the magnitude of W_d is sufficiently small (compared to the centreline velocity of the pipe Poiseuille flow), and relation (3.7) holds as an approximated result. The resulting constrained maximization problem can be reduced to an unconstrained one, by introducing the Lagrange multiplier λ. The functional to be maximized is then

$$F = \omega_i - \lambda \left[\int_0^1 r W_d^2 \mathrm{d}r - \epsilon \right], \tag{3.9}$$

and the necessary condition for optimum is

$$\delta F = \delta\omega_i - 2\lambda \int_0^1 r W_d \delta W_d \mathrm{d}r = 0. \tag{3.10}$$

Substituting the imaginary part of (3.7) into (3.10) results in the following condition for optimum:

$$\delta\omega_i = 2\lambda \int_0^1 r W_d \delta W_d \mathrm{d}r = \mathrm{Re}\left[\frac{\int_0^1 (\delta W_d \mathscr{G} W_d + W_d \mathscr{G} \delta W_d)\mathrm{d}r}{4 \int_0^1 r \boldsymbol{b}_1^* \boldsymbol{D} \boldsymbol{a}_1 \mathrm{d}r} \right]. \tag{3.11}$$

Relation (3.11) must hold for an arbitrary variation δW_d, and thus constitutes the following eigenvalue problem for the eigenvalue λ:

$$\mathrm{Re}\left[\frac{(\mathscr{G} + \mathscr{G}_a) W_d}{4 \int_0^1 r \boldsymbol{b}_1^* \boldsymbol{D} \boldsymbol{a}_1 \mathrm{d}r} \right] - 2\lambda r W_d = 0, \tag{3.12}$$

where $\mathscr{G}_a$ is the adjoint operator of $\mathscr{G}$, based on the inner product $(u, v) \equiv \int_0^1 uv \mathrm{d}r$. Equation (3.12) is given in term of differentiation matrices, for use in numerical calculations, in appendix A.

The eigenvalue problem (3.12) can be solved for any combination of Reynolds numbers (Re) and axial wavenumbers (α), for different eigenvalues ω of the pipe Poiseuille base flow. The operator $\mathscr{G}$ depends on the chosen eigenvalue and the corresponding eigenfunctions (and adjoint eigenfunctions) of the pipe Poiseuille flow. The optimal deviation is the eigenfunction W_m corresponding to the largest eigenvalue λ_m in (3.12).

As mentioned, for the optimization analysis it is assumed that ϵ must be sufficiently small, so that the quadratic terms of W_d in the complete variational system (3.3) have been neglected. Then an approximate deviation solution (for a chosen Poiseuille eigenvalue) could be obtained by (3.12). In order to solve the complete nonlinear system and obtain accurate results, an iterative algorithm is employed. The first iteration is the solution of the reduced system (3.6), and every subsequent iteration exploits the deviation W_d of the previous one to refine the solution to the complete

system (3.3). The algorithm employed for this purpose is

$$W_d^{j+1} = W_d^j - \Omega \left[W_d^j - \frac{W_m^{j+1}}{\sqrt{\left(\int_0^1 r {W_m^{j+1}}^2 \mathrm{d}r \right) / \epsilon}} \right], \tag{3.13}$$

where the superscript j denotes the iteration number and Ω is a relaxation parameter ($0 < \Omega \leqslant 1$). The function W_m is the eigenfunction corresponding to the largest eigenvalue of the following equation:

$$\mathrm{Re} \left[\frac{\left(\mathscr{G}^j + \mathscr{G}_a^j \right) W^{j+1}}{4\Delta^j} \right] - 2\lambda^{j+1} r W^{j+1} = 0, \tag{3.14}$$

where

$$\Delta \equiv \int_0^1 r \boldsymbol{b}_1^* \left(\boldsymbol{D} + \boldsymbol{L}_0 \mathscr{M}_0^{-1} \boldsymbol{D} \mathscr{M}_0^{-1} \boldsymbol{L}_1 + \boldsymbol{L}_2 \mathscr{M}_2^{-1} \boldsymbol{D} \mathscr{M}_2^{-1} \boldsymbol{L}_0 \right) \boldsymbol{a}_1 \mathrm{d}r, \tag{3.15}$$

and the operator $\mathscr{G}$ is computed by solving the eigenvalues and corresponding eigenfunctions of the system (2.10). This system is nonlinear with respect to the eigenvalues ω (the inverse operators on the right-hand side contain the eigenvalues), and hence a Newton–Raphson iterative method is employed to find the least-unstable eigenvalues at each step of the iterative procedure for the optimal deviation. The iterative process given in (3.13) is assumed to converge when the error $\int_0^1 r(W_d^{j+1} - W_d^j)^2 \mathrm{d}r$ is sufficiently small ($\sim 10^{-8}$). The numerical solution of the eigenvalue problem is obtained by the Chebyshev collocation technique. For a sufficiently accurate solution of the eigenvalues, 64–80 polynomials have been used.

The operator $\mathscr{G}$ in (3.7) represents a measure of the sensitivity of each eigenvalue ω to variations in W_d. This operator is the analogue measure to the sensitivity function in the case of axisymmetric deviations, which was introduced by Gavarini *et al.* (2004). Different operators $\mathscr{G}$ can be produced corresponding to the different eigenvalues of the pipe Poiseuille flow. Accordingly, different approximated deviations can be computed with (3.12). However, in the iterative procedure described by (3.13) these approximated deviations are used only as the initial guesses for the nonlinear problem. Since $\mathscr{G}$ has the role of merely indicating the relative efficiency of different eigenfunctions (corresponding to different pipe Poiseuille eigenvalues) to produce a destabilizing base-flow deviation, it is sufficient to consider the diagonal of the equivalent algebraic operator $\boldsymbol{G}$ as a characterizing norm ($\boldsymbol{G}$ is a differentiation matrix used in the numerical calculations, see appendix A). Figure 1 shows the dependence of $|\mathrm{diag}(\boldsymbol{G})|$ on the radial coordinate for the six least-stable modes for $Re = 2000$ and $\alpha = 3.7$ (the plots are normalized by the highest peak among the six modes). The curves in figure 1 (*b*) (for modes 4 and 6) have higher peaks compared to the ones in figure 1 (*a*). Note that the maximum of the curve corresponding to mode 2 is less than half that corresponding to mode 6 in figure 1 (*b*). Therefore, modes 4 and 6 are the most efficient ones (among the six least-stable modes) to start with, as initial guesses to the iterative procedure outlined above. Figure 1 may also imply the approximate location associated with the various deviation solutions. Owing to the nonlinearity of the problem different modes having similar curves in figure 1 may lead to the same converged deviation, e.g. taking mode 2, 4 or 5 as an initial guess may lead to the same solution. The curves corresponding to modes 1 and 3 are located

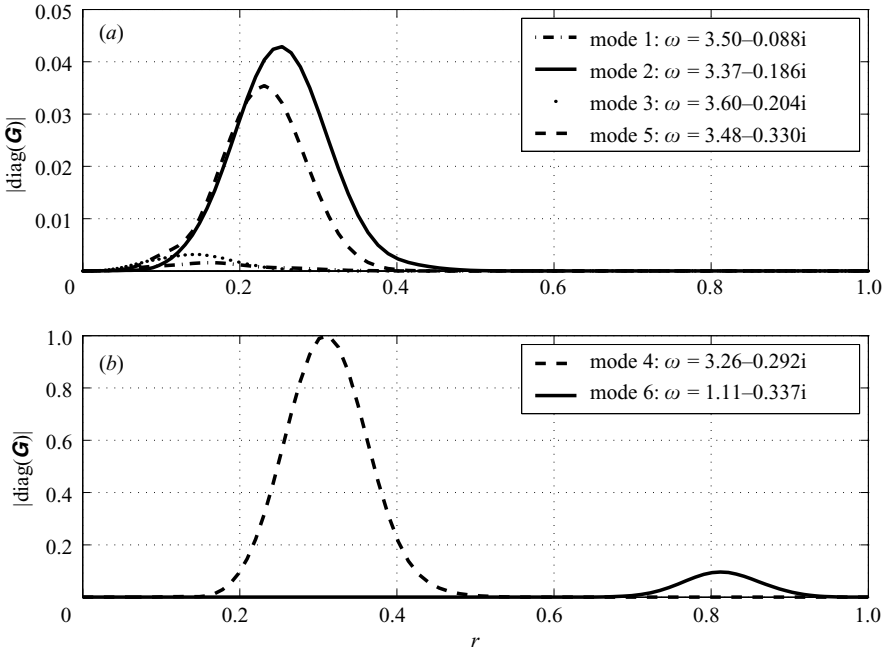

FIGURE 1. Radial distribution of the function $|\mathrm{diag}(\boldsymbol{G})|$ for the six least-stable modes. $Re = 2000$ and $\alpha = 3.7$.

closer to the centreline and might lead to a different solution. However, the curve corresponding to mode 6 is very different from all the others and implies a possible solution close to the wall rather than to the pipe centreline.

In general, higher modes, having higher decay rates, may have larger characterizing norms, i.e. higher peaks in figure 1 (e.g. for the axisymmetric deviations computed by Gavarini *et al.* 2004, mode 22 is shown to have the largest characterizing norm). Thus, higher modes may be more efficient as an initial guess in the iterative process. However, selecting higher modes, which are more sensitive to base-flow deviations, for the role of an initial guess, depends on the magnitude of the deviation: for a sufficiently small base-flow distortion the least-stable modes are always preferable, since the decay rate of higher modes, although more sensitive to the deviations, does not decrease markedly to compete with the decay rate decrease of the least-stable modes. On the other hand, for larger distortions, which are capable of attracting higher modes to become the most unstable ones, it would be relevant to consider additional higher modes in figure 1, in order to choose the most efficient initial guess in the iterative analysis. In the present study relatively small deviations have been considered, such that the first six least-stable modes have been the most efficient initial guesses in the iterative procedure.

It should be noted that the optimal base-flow deviations found with the analysis outlined above do not satisfy the governing Navier–Stokes equations. A weak dependence of the deviation on the axial coordinate and time must therefore exist in order to satisfy the viscosity terms of the momentum equations, and is neglected in the present analysis (see also Bottaro *et al.* 2003 for similar arguments regarding two-dimensional deviations in channels flows). Moreover, it is important to mention in this context that the deviations are not subjected to a constraint on the cross-section mass flux. Nevertheless, the average velocity difference between the Poiseuille

parabolic profile and the distorted profile is less than $O(10^{-8})$ for all Reynolds numbers considered throughout the analysis.

4. Results

In the following, relevant results for optimal axisymmetric deviations are first presented in § 4.1, mainly for comparison. The optimal azimuthally periodic deviation results follow in § 4.2, and § 4.3 presents results of the flow induced by nonlinear interactions between the unstable waves resulting from the azimuthally periodic deviations.

4.1. *Optimal axisymmetric deviations*

As mentioned above, the axisymmetric deviation analysis was first carried out by Gavarini *et al.* (2004), who analysed spatial unstable disturbances; additional conclusions regarding pipe flow stability have been drawn recently by Ben-Dov & Cohen (2007). The results for this case could be produced with a simpler mathematical procedure than the azimuthally periodic deviation analysis. Therefore, it is instructive to explore the results in this case, before proceeding to a careful examination of the non-axisymmetric deviation results. The mathematical formulation for obtaining the results in the present subsection can be found in Gavarini *et al.* (2004) for spatial instability and in Ben-Dov (2006) for the temporal case.

Ben-Dov & Cohen (2007) have solved the optimal axisymmetric deviations for different Reynolds numbers (Re) and axial wavenumbers (α), for the azimuthal wavenumber $n=1$. The constraint represented by ϵ has been computed to yield neutral stability. For a given deviation the cross-section energy density is defined as the energy per unit pipe length added to the flow as a result of the additional deviation:

$$E = \int_0^{2\pi} \int_0^1 r\left[(W_p + W_d)^2 - W_p^2\right] \mathrm{d}r\,\mathrm{d}\theta = 2\pi \int_0^1 r\, W_d(2W_p + W_d)\mathrm{d}r, \qquad (4.1)$$

where W_d denotes the axisymmetric deviation from the pipe Poiseuille profile.

Figure 2 (a) presents the cross-sectional energy density of the optimal deviations, yielding neutral stability ($E = E_n$), as a function of α for four different Reynolds numbers. For sufficiently low Reynolds numbers ($Re < 600$) only one optimal deviation exists. On increasing the Reynolds number slightly above 600 a bifurcation occurs and two optimal deviation solutions (branches) co-exist (as presented in the figure for $Re \geqslant 1200$). Generally, as the Reynolds number is further increased the energy density of the optimal deviation required to trigger instability is decreased, and additional bifurcations are expected to take place. In the limit of $Re \to \infty$ the deviation magnitude is considered to be infinitesimal and the accurate deviation is computed solely by equation (3.12), without the need of the iterative procedure. Therefore, in this limit of $\epsilon \to 0$ an infinite number of deviation solutions exists, corresponding to the infinite number of eigenvalues associated with the pipe Poiseuille profile.

Figure 2 (b) presents the optimal deviation radial distributions of the curves in figure 2 (a), corresponding to the local minima at which $\alpha = \alpha_{min}$. The solid lines correspond to the minima of the lower α_{min} branch of solutions, whereas the dashed lines correspond to the minima of the higher α_{min} branch. As the Reynolds number is increased it can be seen that for the lower α_{min} solutions the deviations tend to be localized next to the pipe wall, whereas for the higher α_{min} branch the deviations tend to be located around the centreline.

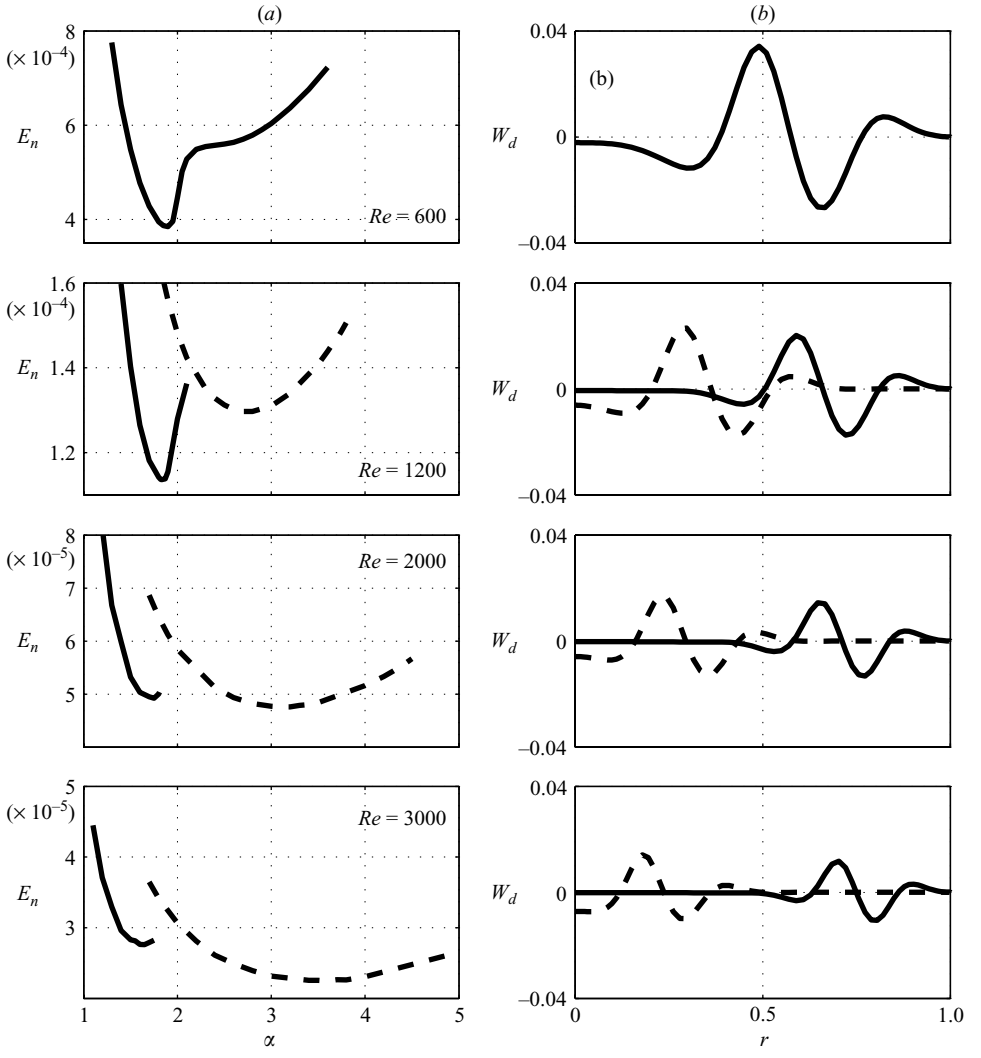

FIGURE 2. (*a*) Curves of deviation energy density yielding a neutral stability (E_n) vs. axial wavenumber (α) for various Reynolds numbers. For $Re = 600$ only one branch of the optimal deviation exists, whereas for Re above 600 two branches are presented. (*b*) The optimal deviation radial distributions corresponding to the minima of the curves in (*a*).

In figure 2 (*a*) it can be noticed that for Reynolds numbers up to approximately 2000 the global minimum energy solution is the one located near the wall, whereas for values above $Re \approx 2000$ the solution located around the centreline becomes the one having the global minimum energy, and therefore is more likely to trigger an exponential instability. A more accurate value for this 'critical' Reynolds number has been found by Ben-Dov & Cohen (2007) to be $Re = 1840$. The subcritical solution (having the minimum energy below $Re = 1840$) generates unstable waves which have about twice the wavelength of the supercritical waves (having the minimum energy above $Re = 1840$), and their time scale is approximately 3.5 times longer. These two characteristics may provide an explanation for the preference of the solution having a global minimum of energy density above $Re = 1840$ to be the one leading to transition.

If the deviation persists over a sufficiently long time and spatial extent, compared to the respective scales of the unstable waves, these waves can grow and initiate transition. (It should be noted that the length and time scales of the deviation are assumed in the analysis to be infinite.) We therefore propose to associate this 'critical' Reynolds number with known findings, in which transition has been observed only for Reynolds numbers above approximately 1800 (e.g. see the experiments by Darbyshire & Mullin 1995 and more recently by Peixinho & Mullin 2006, and the supporting results of the direct numerical simulations by Willis & Kerswell 2007).

4.2. *Optimal azimuthally periodic deviations*

The energy density and the corresponding optimal functions W_d have been determined for various Reynolds numbers and a range of axial wavenumbers. The energy density associated with the azimuthally periodic deviation is given by

$$E = \int_0^{2\pi} \int_0^1 r\left\{[W_p + W_d\cos(\theta)]^2 - W_p^2\right\}\mathrm{d}r\mathrm{d}\theta = \pi\int_0^1 r W_d^2\mathrm{d}r, \tag{4.2}$$

where W_d is the radial distribution of the deviation.

We first recall that in the analysis described above, the eigenfunctions series in (2.3) is truncated and all terms having $|n| > 2$ are omitted. In order to verify that the higher terms are indeed negligible and the series is converged with the terms with indices satisfying $|n| \leqslant 2$, the analysis for solving the eigenvalue problem has been expanded by including the terms with indices $|n| \leqslant 3$. The expanded equations are given in appendix B. Note that for small magnitudes of W_d (relative to the Poiseuille profile) the error in this case is of $O(|W_d|^4)$, while for the series including the indices $|n| \leqslant 2$ the error is of $O(|W_d|^2)$. Figure 3 presents curves of the optimal deviation energy density which yields neutral stability of waves ($E = E_n$) versus the axial wavenumber α at four different Reynolds numbers. The solid lines correspond to the series $|n| \leqslant 2$ and the dashed lines correspond to the series $|n| \leqslant 3$. The maximum error (for all Reynolds numbers) is about 3%. Since the error is sufficiently small the series with indices $|n| \leqslant 2$ is used in the following.

In figure 4 curves of the optimal deviation energy density versus the axial wavenumber (α), which trigger a neutral stability, are shown for eight different Reynolds numbers. For Reynolds numbers below 200 a single solution is found (solid line). At a Reynolds number slightly above $Re = 200$ a bifurcation to another solution appears, and for $Re = 250$ two different solutions can be seen on figure 4 (a) (the second branch of solutions is denoted by the dashed line). As the Reynolds number is further increased the upper branch of solutions bifurcates again at a Reynolds number slightly above 500 (see figure 4(b)), and another branch is formed (dashed-dotted line). At $Re = 600$ three solutions co-exist. In figure 4(c) we can see that on further increasing the Reynolds number the upper branch tends towards values of α_{min} similar to those of the two other branches. However, the energy density difference between the upper branch (dashed line) and the two others (solid and dashed-dotted lines) increases, whereas the difference between the lower (solid line) and the middle (dashed-dotted line) branches decreases.

Figure 5 presents the optimal deviation radial distributions for the minima of the curves shown in figure 4. The lower α_{min} branch (solid lines) tends to be localized near the centreline, whereas the upper α_{min} branch (dashed lines) tends to be localized next to the wall. As the Reynolds number is increased the lower and upper α_{min} deviations tend to move further towards the centreline and the wall, respectively. The dashed-dotted line, corresponding to the middle α_{min} branch, is located closer to the

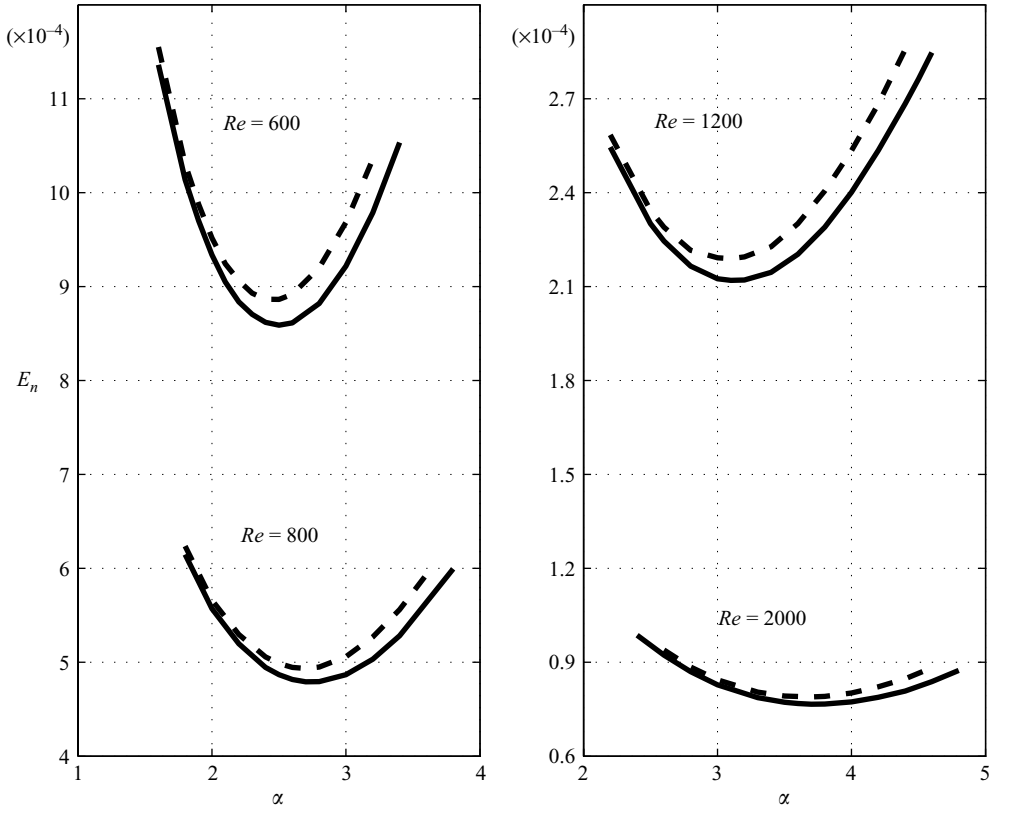

FIGURE 3. Curves of deviation energy density yielding a neutral stability (E_n) vs. axial wavenumber (α) for various Reynolds numbers; solid lines correspond to solutions including $|n| \leqslant 2$ terms and dashed lines to more accurate solutions including $|n| \leqslant 3$ terms.

centreline as the Reynolds number is increased, and therefore is more similar to the lower branch, denoted by the solid line. It is clear from figures 4 and 5 that for each branch of solution (among the three presented), when the deviations occupy a circular region closer to the centreline their minimum energy is lower than those occupying an annulus closer to the pipe wall. This result is due to the cylindrical geometry, for which the energy density associated with a radial width occupied by a certain deviation (required to trigger an inflectional instability) is lower for a deviation located within an annular cross-section closer to the centreline than for a deviation closer to the wall.

A comparison between the azimuthally periodic deviation solutions presented in figure 4 and the axisymmetric ones shown in figure 2, having the same Reynolds number, indicates that the energy density required for the optimal azimuthally periodic deviations to trigger an exponential instability is almost twice the energy required in the axisymmetric case. Unlike the axisymmetric deviation, the azimuthally periodic deviation energy density in (4.2) is independent of the Poiseuille base flow. Note that for axisymmetric deviations the energy density given by (4.1) includes an additional contribution (having a negative sign) representing the energy transferred to the deviation from the Poiseuille base flow. Thus, unlike the axisymmetric deviations, in the case of azimuthally periodic deviations energy is not transferred from the base

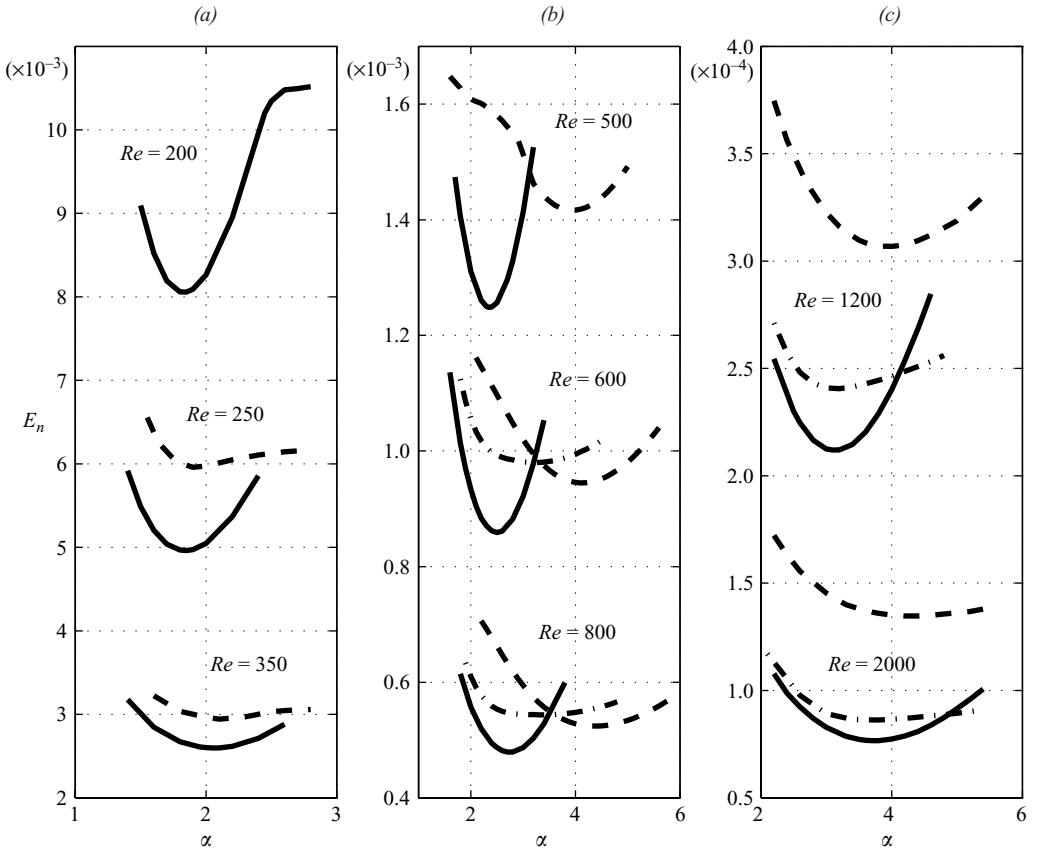

FIGURE 4. Curves of deviation energy density yielding a neutral stability (E_n) vs. axial wavenumber (α) for various Reynolds numbers. For $Re \leqslant 200$ only one branch of the optimal deviation exists (denoted by the solid line), for $250 \leqslant Re \leqslant 500$ two branches are presented (the second bifurcated solution is denoted by the dashed line), and for $Re \geqslant 600$ three branches are presented (the third bifurcated branch is denoted by the dashed-dotted line).

flow to reduce the deviation amplitude. This difference also exists for all deviations having higher azimuthal periodicity.

Figure 6 presents the deviation velocity in the cross-sectional plane for the centreline and near-wall deviation radial distributions presented in figure 5 at $Re = 2000$ (denoted by solid and dashed lines, respectively). The deviation velocity is indicated by a grey scale, where light and dark are for higher and lower velocities, respectively. The velocity is normalized by the maximum deviation velocity. For both deviations, localized regions of low and high speeds next to the centreline (in figure 6*a*) or next to the wall (in figure 6b) can be noticed. These structures have a strong resemblance to streaks, often observed next to the wall during transition in wall-bounded shear flows (e.g., see Elofsson & Alfredsson 1998).

In figure 7(*a*) the relation between the minimum energy density and the Reynolds number for the lower $\alpha_{\min}$ branch is shown. The corresponding relation between $\min(E_n)$ and its associated axial wavenumber α_{min} is shown in figure 7(*b*). The scaling of the minimum deviation amplitude (square root of the minimum energy density) with the Reynolds number is $O(Re^{-1})$. This result is identical to the scaling of the

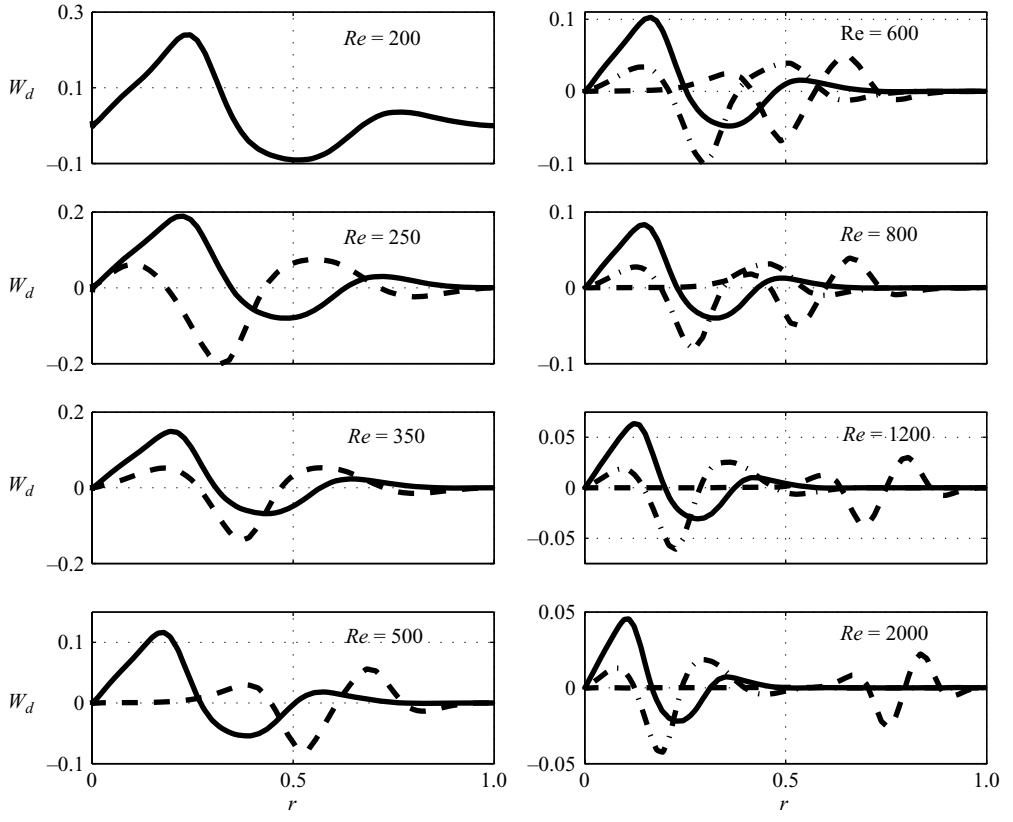

FIGURE 5. Optimal deviation distributions corresponding to the local minima of the curves in figure 4 ($\alpha = \alpha_{min}$) for various Reynolds numbers. The solid lines correspond to the lower α_{min} branch, the dashed lines to the higher α_{min} branch, and the dashed-dotted lines to the middle α_{min} branch.

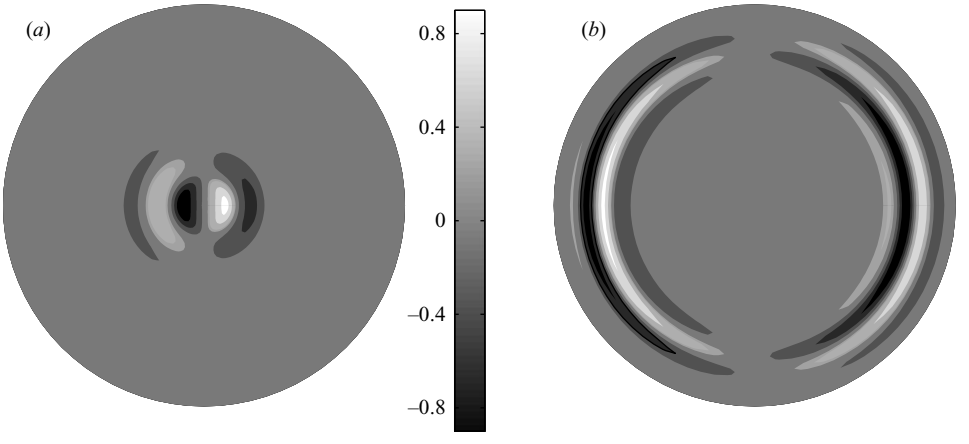

FIGURE 6. Optimal deviations in the pipe cross-sectional plane for $Re = 2000$. (*a*) Centreline deviation, corresponding to the lower α_{min} branch ($\alpha = 3.7$) and (*b*) near-wall deviation, corresponding to the higher α_{min} branch ($\alpha = 4.3$). The velocity is normalized by the maximum deviation velocity.

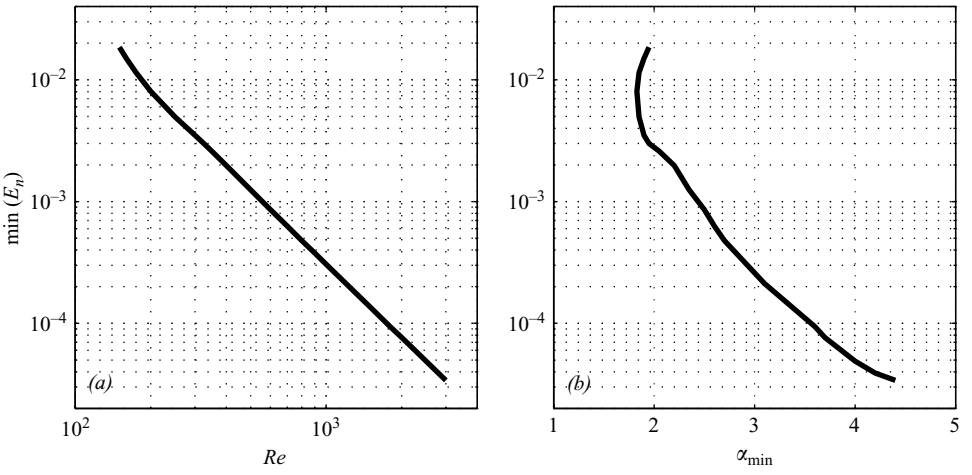

FIGURE 7. (*a*) Minimum energy density as a function of the Reynolds number for the lower α_{min} branch and (*b*) the corresponding axial wavenumber.

axisymmetric deviations (shown in figure 15 in Gavarini *et al.* 2004), and has been observed in experiments by Hof *et al.* (2003). It should be noted that the same scaling and a very similar behaviour of the relation between the minimum energy density and α_{min} (in figure 7*b*) have been shown by Bottaro *et al.* (2003) to hold for plane Couette flow.

Figure 8 presents the cross-sectional distribution of the exponential modes velocity field for two Reynolds numbers ($Re = 800$ and $Re = 2000$). The left-hand plots correspond to the lower α_{min} solution (figures 8*a* and 8*c*), whereas the right-hand ones correspond to the higher α_{min} solution (figures 8*b* and 8*d*). The velocity components in the, (r, θ)-plane are indicated by arrows and the axial velocity is indicated by the grey scale, where light or dark signifies velocities higher or lower than the base flow, respectively. The figure is plotted for an arbitrary pipe cross-section (for a certain phase $\alpha z - \omega t$). In the left-hand plots a pattern of two counter-rotating vortices next to the centreline can be noticed. The right-hand plots show that the deviations next to the wall induce a region of concentrated vorticity along a section of the wall. For the lower Reynolds number ($Re = 800$) the low- and high-speed regions are distant from the wall, whereas for the higher Reynolds number ($Re = 2000$), which is more characteristic of a transition scenario, they are attached to the pipe wall. These regions represent travelling waves along the wall. The two studies by Wedin & Kerswell (2004) and by Faisst & Eckhardt (2003) present similar travelling wave patterns for higher orders of symmetries. The wave patterns in these cases, however, represent nonlinear wave solutions of the governing equations, and it is believed that these symmetrical patterns could be obtained as a result of the growth of waves triggered by azimuthally periodic deviations of higher orders, i.e. for $m > 1$, where the deviation is then given by $W_d(r)\cos(m\theta)$ (the present work is restricted to $m = 1$).

4.3. *Nonlinear interactions of unstable waves*

The linear instability of the azimuthally periodic distorted base flow yields exponentially growing waves which may interact through the nonlinear terms of the Navier–Stokes equations, and consequently induce a modified, azimuthally dependent mean flow in the cross-sectional plane. This process has been demonstrated theoretically and experimentally by Cohen & Wygnanski (1987) for an axisymmetric jet flow

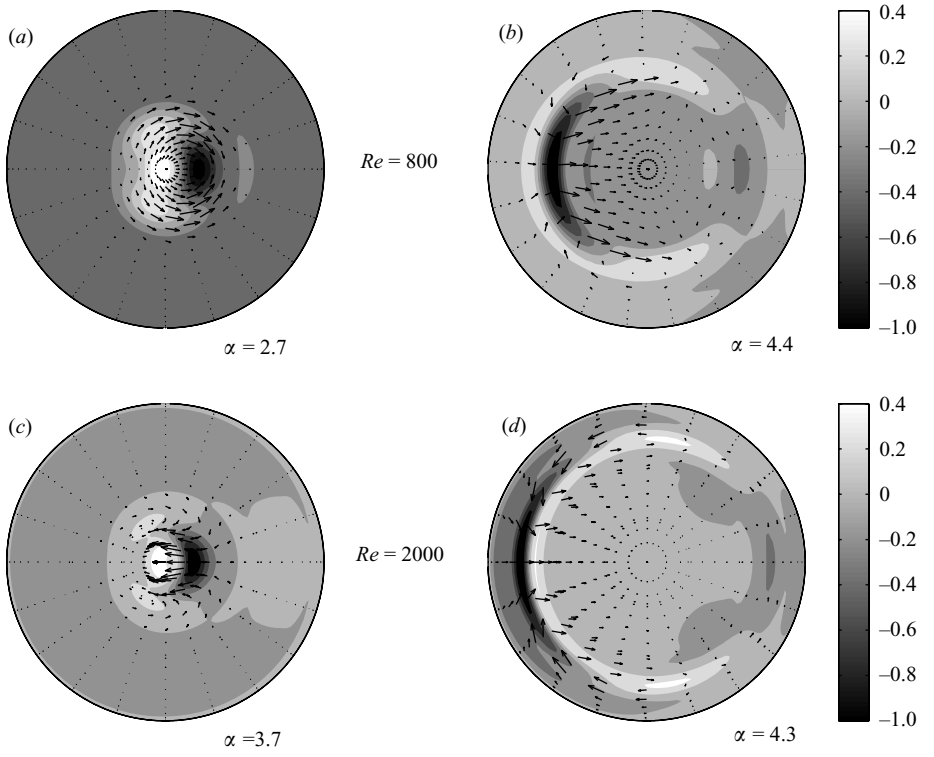

FIGURE 8. The exponential-modes velocity field for (*a*,*b*) $Re = 800$ and (*c*,*d*) $Re = 2000$. The left-hand plots (*a*,*c*) correspond to the lower α_{min} solution ($\alpha_{min} = 2.7$ for $Re = 800$, $\alpha_{min} = 3.7$ for $Re = 2000$), and the right-hand ones (*b*,*d*) correspond to the higher α_{min} solution ($\alpha_{min} = 4.4$ for $Re = 800$, $\alpha_{min} = 4.3$ for $Re = 2000$). Cross-sectional velocity is indicated by arrows and axial velocity by a grey scale, where light and dark are for higher and lower velocities, respectively.

resulting from the nonlinear interaction between two azimuthal waves. Waleffe (1995, 1997) presented a similar analysis as part of a self-sustaining process in wall-bounded flows, and Wedin & Kerswell (2004) applied this analysis to pipe flow.

The equations governing the flow induced by forcing unstable waves are derived as follows. The total flow $\{u + U, v + V, w + W, p + P\}$, where $\{u, v, w, p\}$ denotes the unstable wave velocity and pressure and $\{U, V, W, P\}$ denotes the induced mean flow field, is substituted into the Navier–Stokes equations. Then the equations are averaged over the axial direction and over time, and the nonlinear terms associated with the induced flow are neglected by assuming they are of a small order of magnitude. The resulting set of equations is then

$$\frac{\partial (rU)}{\partial r} + \frac{\partial V}{\partial \theta} = 0, \tag{4.3a}$$

$$\frac{1}{Re}\left(\nabla_\perp^2 U - \frac{U}{r^2} - \frac{2}{r^2}\frac{\partial V}{\partial \theta}\right) - \frac{\partial P}{\partial r} = \left\langle u\frac{\partial u}{\partial r} + \frac{v}{r}\frac{\partial u}{\partial \theta} + w\frac{\partial u}{\partial z} - \frac{v^2}{r}\right\rangle, \tag{4.3b}$$

$$\frac{1}{Re}\left(\nabla_\perp^2 V - \frac{V}{r^2} + \frac{2}{r^2}\frac{\partial U}{\partial \theta}\right) - \frac{1}{r}\frac{\partial P}{\partial \theta} = \left\langle u\frac{\partial v}{\partial r} + \frac{v}{r}\frac{\partial v}{\partial \theta} + w\frac{\partial v}{\partial z} + \frac{uv}{r}\right\rangle, \tag{4.3c}$$

$$\frac{1}{Re}\nabla_\perp^2 W = \left\langle u\frac{\partial w}{\partial r} + \frac{v}{r}\frac{\partial w}{\partial \theta} + w\frac{\partial w}{\partial z}\right\rangle, \tag{4.3d}$$

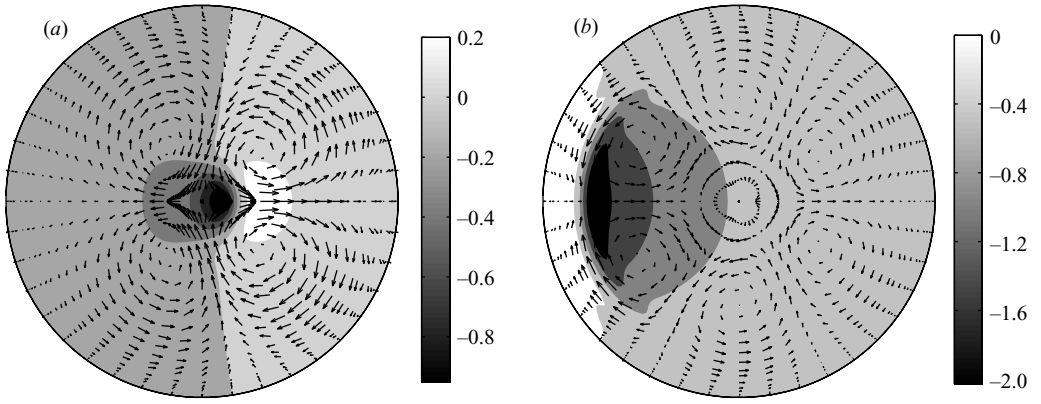

FIGURE 9. Velocity field as a result of nonlinear interactions between the unstable waves (at $Re = 2000$) for (a) the near-centreline deviation ($\alpha = 3.7$) and for (b) the near-wall deviation ($\alpha = 4.3$). Cross-sectional velocity is indicated by arrows and axial velocity by a grey scale, where light and dark are for higher and lower velocities, respectively.

where

$$\nabla_{\perp}^2 = \frac{1}{r}\frac{\partial}{\partial r}\left(r\frac{\partial}{\partial r}\right) + \frac{1}{r^2}\frac{\partial^2}{\partial \theta^2},$$

and the brackets $\langle\ \rangle$ denote an average in the axial direction z and in time t. On the right-hand side of (4.3) u, v and w stand for the velocities associated with the most unstable mode only. Since the converged solutions for the unstable waves are given by the series (2.3) for $|n| \leqslant 2$, the solution to the set (4.3) may be expressed by the series

$$\{U, V, W, P\} = \sum_{n=-4}^{4} \{U_n(r), V_n(r), W_n(r), P_n(r)\} \mathrm{e}^{\mathrm{i}n\theta}. \tag{4.4}$$

Substituting (4.4) into the left-hand side of (4.3), together with an unstable wave solution into the forcing terms on the right-hand side, provides a system of four ordinary equations. Note that the subset (4.3a)–(4.3c) for the cross-sectional velocity and the single equation (4.3d) for the axial velocity are solved independently of each other. The cross-sectional velocity equations have been solved by Wedin & Kerswell (2004) for self-interacting travelling wave solutions. Their analysis showed an efficient nonlinear feedback to streamwise rolls structures similar to the ones initially leading to the travelling waves.

Figure 9 presents the solution of the set (4.3a)–(4.3c) for the cross-sectional velocity components U and V (indicated by the arrows), and of equation (4.3d) for the axial velocity W (indicted by the grey scale). In figure 9(a) the induced flow is a result of forcing terms consisting of the near-centreline deviation at $Re = 2000$ (the minimum energy deviation for $\alpha = 3.7$), whereas figure 9(b) is the induced flow resulting from the near-wall deviation at the same Reynolds number (where the minimum energy deviation is for $\alpha = 4.3$). The axial velocity in the figures is normalized by the average of the cross-sectional velocity magnitude. Thus, it can be seen that the maximum (absolute) axial velocity in figure 9(a) is slightly less than the average magnitude of the cross-sectional velocity. The average magnitude of the axial velocity in this figure is 0.07 of the average magnitude of the cross-sectional velocity. This ratio signifies the modulation of the axial velocity deviation to an almost pure cross-sectional velocity

field (through nonlinear self-interactions of the travelling waves resulting from the deviation). This result is consistent with the feedback scenario suggested by Waleffe (1995, 1997) and demonstrated by Wedin & Kerswell (2004) in pipe flow. Figure 9(*b*) shows a less efficient feedback mechanism. In this case the ratio between the average magnitudes of the axial velocity and the cross-sectional velocity is 0.3.

The cross-sectional flow field in figures 9(*a*) and 9(*b*) consists of streamwise rolls. In figure 9(*a*) four rolls can be seen, whereas in figure 9(*b*) six rolls can be seen around the centreline, although they seem to be weaker than the ones in figure 9(*a*). The roll structure in both figures implies that the deviations, which may be formed initially by pairs of streamwise rolls, may lead to higher symmetries of streamwise rolls. Similar cross-sectional symmetries have been presented by Faisst & Eckhardt (2003) and by Wedin & Kerswell (2004) for travelling wave solutions. These coherent structures are discussed widely in the review papers by Kerswell (2005) and by Eckhardt *et al.* (2007). A very similar pattern of counter-rotating vortices and high-speed streaks has also been shown numerically by Schneider, Eckhardt & Yorke (2007) to appear when pipe flow transition is triggered by sufficiently large perturbations.

5. Discussion

The results in the present study demonstrate that very small finite-amplitude three-dimensional deviations from the developed base flow in a pipe render instability. For an azimuthally periodic velocity deviation leading to instability, the minimal magnitude of the deviation has been found to be approximately $20/Re$ (see figure 7*a*). Although the finite-amplitude deviations are small in magnitude, compared to the pipe Poiseuille base flow, the problem is highly nonlinear and, owing to bifurcations of the optimal deviation solutions, multiple solutions of azimuthally periodic deviations are found.

The first appearance of multiple deviation solutions occurs at Reynolds numbers as low as 200 (see figure 4), and as the Reynolds number is increased more solutions can be traced by finding more bifurcation points. The question then is, physically what would be the minimal Reynolds number for which such deviations may be formed in the flow and trigger instability, and thus have a role in a transition scenario. It is not obvious that the deviation solutions found through the optimization analysis can actually be formed in the flow. In order for such deviations to act two conditions must be fulfilled: first there must be some external forcing, which supplies the energy required to form the deviation; secondly, the deviations must persist for a sufficiently long axial distance and time compared to the characteristic length and time scales of the growing unstable waves which are triggered by them.

These two conditions are not independent of each other, since the mechanism leading to the formations of such deviations also determines the length and time scales of their persistence in the flow. In any case, the probability of an optimized unstable finite deviation existing in the flow increases as the Reynolds number is increased, since the energy required to create the deviation decreases. Moreover, as the Reynolds number is increased towards ≈ 2000 the optimal deviation becomes more localized in the radial direction (see figure 5), signifying a more likely consequence of localized disturbances which are typical in bounded flows (e.g.wall roughness). In general, one can think of two optional scenarios for the creation of finite-amplitude deviations in the flow: they can be a consequence of large persistent forcing which forms them directly, or they can be produced by a transient growth amplification of smaller initial disturbances, due to the non-normality of the Navier–Stokes operator

(see Biau & Bottaro 2004 for a detailed discussion on these two scenarios in bounded shear flows).

The first scenario of deviation formation is more likely to produce axisymmetric deviations, since this requires less energy (almost 50%) than the azimuthally periodic ones. This is because, unlike the axisymmetric deviation, the azimuthally periodic deviation energy density, represented by (4.2), is independent of the Poiseuille base flow. For axisymmetric deviations the energy density, given by (4.1), includes an additional negative contribution, representing the energy transferred to the deviation from the Poiseuille base flow.

The second scenario, which has been the basic motivation for considering non-axisymmetric deviations in the present work, is the formation of an azimuthally periodic deviation from an initial disturbance by a transient growth amplification, a mechanism which is related to the non-normality of the governing equations. Accordingly, as the Reynolds number is increased, larger amplification of certain kinds of initial disturbances is produced. The type of initial disturbances experiencing the most significant transient growth is characterized by a crossflow velocity. Such an initial velocity yields an amplified (non-axisymmetric) streamwise velocity, a pattern which is often termed 'streaks'. Among all azimuthally periodic initial disturbances the most amplified ones are known to have a periodicity of the form $\cos(\theta)$ (e.g. see Bergström 1993 and Schmid & Henningson 1994). The transient growth amplification is characterized by a relatively long length and time scales compared to the resulting unstable growing waves; the length scale of the transient growth amplification of an initial disturbance is of $O(1/\varepsilon)$, where ε denotes the magnitude of the initial disturbance. Therefore, for ε much smaller in magnitude than $O(1)$ the characteristic length scale of the transient amplification is much larger than $O(1)$, whereas the length scale of the resulting unstable waves, according to figure 7(b), is $2\pi/\alpha \sim O(1)$. Since the deviations are of the magnitude of approximately $20/Re$, and the initial disturbance leading to them is assumed to be even smaller, the length scale of the transient amplification leading to the deviation is much larger than $O(1)$. The same estimation holds for the time-scale difference between the transient amplification leading to the deviations and the resulting unstable waves. Hence, the mechanism of the transient growth amplification which leads to azimuthally periodic deviations may compete with the mechanism shown for the lower energy axisymmetric deviations (which has been recently suggested by Ben-Dov & Cohen 2007 to explain transition at $Re \approx 2000$).

Finding an approximated initial disturbance flow field, which may lead to azimuthally periodic deviations, is possible in the case in which the transient evolution of this initial disturbance is mainly governed by inertial effects and viscosity is negligible (otherwise the initial value problem expressed by the Navier–Stokes operator is ill-posed). The initial disturbances in such cases are known to have a structure of streamwise rolls in the pipe cross-sectional plane. Optimal deviations, however, which are localized in the cross-sectional plane, have high velocity gradients. Therefore, the diffusion of momentum (through viscosity) of any kind of small initial disturbance is crucial during the transient amplification towards the formation of a non-axisymmetric deviation. Thus, finding an initial disturbance, leading to an optimal deviation, is a difficult task which was not attempted within the scope of this paper.

The unstable waves, emerging from the base flow distorted by the optimal azimuthally periodic deviations, may self-interact and induce a flow field in the pipe cross-section which is independent of the axial direction and time. The solutions of the flow induced by these self-interactions show that most of the energy associated

with the axial velocity is likely to be modulated to a cross-sectional velocity field. This modulation appears to be stronger for optimal deviations around the centreline. As mentioned above, the azimuthally periodic deviations may be a result of an initial cross-sectional velocity field, and therefore a modulation of the axial velocity deviations back to a cross-sectional velocity field implies a possible feedback mechanism, as part of a self-sustaining process which has been suggested by Waleffe (1995, 1997) and demonstrated by Wedin & Kerswell (2004) in pipe flow. The cross-sectional flow induced by the nonlinear unstable wave interactions consists of streamwise rolls having high circumferential symmetries, which may lead to deviations consisting of higher azimuthal modes. The experiments by Eliahou *et al.* (1998), in which they introduced into a developed pipe flow different periodic disturbances, showed that transition occurred most efficiently (i.e. required the smallest external disturbance amplitudes) for azimuthally periodic distortions of the base flow. The distortions with $m = 2$, where m denotes the azimuthal periodicity of the deviation (excited by $n = \pm 1$ modes), lead to transition with relatively small disturbance amplitudes. However, the distortions consisting of the azimuthal periodicity $m = 4$ (excited by $n = \pm 2$ modes) were seen to be the most efficient leading to transition. Further supporting evidence for the significance of azimuthally periodic distortions having higher m-periodicity is the travelling wave structures found independently by Faisst & Eckhardt (2003) and Wedin & Kerswell (2004). These structures have also been observed experimentally and computationally by Hof *et al.* (2004).

The results for the nonlinear self-interactions of the unstable waves, which showed the formation of highly symmetrical streamwise rolls, the travelling wave solutions found by Faisst & Eckhardt (2003) and Wedin & Kerswell (2004), and the above-mentioned experimental result by Eliahou *et al.* (1998), imply that an analysis for higher azimuthal periodicity deviations (especially for $m = 2$ or $m = 4$) may be valuable. The method derived in this study is the basis for such future work and a similar derivation to optimal oblique deviations in channel flows may also be based on the present method.

6. Concluding remarks

In this study we have derived a method for finding optimal azimuthally periodic deviations which render a pipe flow unstable. The minimal magnitude of an azimuthally periodic velocity deviation (proportional to $\cos(\theta)$), which triggers instability, is approximately $20/Re$. Thus, it is evident that very low-energy-density streak-like structures, which are linearly unstable, may exist in the flow. The energy density required for such streaks to become unstable has been found to be, however, larger than that required for axisymmetric deviations to destabilize the flow (almost double). Nevertheless, azimuthally periodic and axisymmetric deviations may be two different paths to transition.

At high Reynolds numbers ($Re \sim 10^3$) multiple deviation solutions exist. They have a localized structure, and occupy less than a half of the pipe cross-section. When the deviation is closer to the centreline a lower energy is required in order to trigger instability (due to a more efficient inflectional instability).

The nonlinear self-interactions between the growing waves, resulting from the distorted base flow, lead to a modulation of the axial flow in a cross-sectional velocity field. Since the deviations may be a result of an initial cross-sectional velocity, a possible feedback mechanism is implied, as part of a self-sustaining process.

The authors would like to thank Anatoli Tumin and Orkan M. Umurhan for fruitful discussions regarding § 5 and Alessandro Bottaro for a discussion on the optimal axisymmetric deviation method. The authors also thank Jimmy Philip and Josef Tanny for their careful reading of the manuscript and valuable comments.

Appendix A. Differential operators in terms of differentiation matrices

The analysis in § 2 and § 3 involves inverse differential operators, which cannot be expressed analytically. However, it is possible to deal with them in algebraic form, i.e. by discretizing the differential operators which are then represented by approximated matrices. Then expressing an inverse operator simply requires inverting its corresponding approximated matrix. In the spectral collocation techniques differential operators are represented by approximated differentiation matrices.

Expressing the differential eigenvalue problem (3.12) in terms of matrices gives

$$\mathrm{Re}\left(\frac{\boldsymbol{G}+\boldsymbol{G}^{T}}{4\displaystyle\int_{0}^{1} r\boldsymbol{b}_{1}^{*}\boldsymbol{D}\boldsymbol{a}_{1}\mathrm{d}r}\right)-2\lambda\boldsymbol{r}=0, \tag{A 1}$$

where $\boldsymbol{G}$ denotes a differentiation matrix, representing the differential operator $\mathscr{G}$. The notation $\boldsymbol{r}$ in the second term on the left-hand side of (A 1) denotes a diagonal matrix with the elements of the discretized radial coordinate r. Note that $\mathrm{Re}(\boldsymbol{G}+\boldsymbol{G}^{T})$ is a symmetric matrix and $\boldsymbol{r}$ is a symmetric positive definite matrix, and therefore the eigenvalues and eigenvectors of (A 1) are necessarily real.

The operator $\mathscr{G}$ in (3.7) is constructed by taking the inner product, according to (3.4), of the terms inside the brackets on the right-hand side of (3.6). For convenience we denote the inverse operators $\mathscr{M}_{0}^{-1}$ and $\mathscr{M}_{2}^{-1}$ by the 4×4 matrices $\boldsymbol{A}=\{\boldsymbol{A}_{ij}\}$ and $\boldsymbol{B}=\{\boldsymbol{B}_{ij}\}$, respectively, where each element represents a differentiation matrix. After matrix multiplications and integration by parts of the terms W_{d}' and $\delta W_{d}'$, the following matrix $\boldsymbol{G}$ is obtained for the operator $\mathscr{G}$:

$$\begin{aligned}\boldsymbol{G}=\;&\mathrm{i}\alpha\boldsymbol{r}\boldsymbol{v}_{1a}^{*}\{\mathrm{i}\alpha(2\boldsymbol{A}_{12}+\boldsymbol{B}_{12})\boldsymbol{u}_{1}+(2\boldsymbol{A}_{14}+\boldsymbol{B}_{14})(\boldsymbol{u}_{1}\boldsymbol{\partial}+\mathrm{i}\alpha\boldsymbol{w}_{1})+\mathrm{i}[\alpha\boldsymbol{B}_{13}+(\boldsymbol{B}_{14}-2\boldsymbol{A}_{14})\boldsymbol{r}^{-1}]\boldsymbol{v}_{1}\}\\&+\mathrm{i}\alpha\boldsymbol{r}\boldsymbol{w}_{1a}^{*}\{\mathrm{i}\alpha(2\boldsymbol{A}_{22}+\boldsymbol{B}_{22})\boldsymbol{u}_{1}+(2\boldsymbol{A}_{24}+\boldsymbol{B}_{24})(\boldsymbol{u}_{1}\boldsymbol{\partial}+\mathrm{i}\alpha\boldsymbol{w}_{1})+\mathrm{i}[\alpha\boldsymbol{B}_{23}+(\boldsymbol{B}_{24}-2\boldsymbol{A}_{24})\boldsymbol{r}^{-1}]\boldsymbol{v}_{1}\}\\&+\boldsymbol{p}_{1a}^{*}\{\alpha[(\boldsymbol{B}_{22}-2\boldsymbol{A}_{22})-\alpha\boldsymbol{r}(2\boldsymbol{A}_{32}+\boldsymbol{B}_{32})]\boldsymbol{u}_{1}+\mathrm{i}[(2\boldsymbol{A}_{24}-\boldsymbol{B}_{24})+\alpha\boldsymbol{r}(2\boldsymbol{A}_{34}+\boldsymbol{B}_{34})](\boldsymbol{u}_{1}\boldsymbol{\partial}\\&+\mathrm{i}\alpha\boldsymbol{w}_{1})+[(2\boldsymbol{A}_{24}+\boldsymbol{B}_{24})\boldsymbol{r}^{-1}+\alpha\boldsymbol{r}(2\boldsymbol{A}_{34}-\boldsymbol{B}_{34})\boldsymbol{r}^{-1}-\alpha(\alpha\boldsymbol{r}\boldsymbol{B}_{33}-\boldsymbol{B}_{23})]\boldsymbol{v}_{1}\}\\&-\boldsymbol{\partial}\boldsymbol{r}\boldsymbol{p}_{1a}^{*}\{\mathrm{i}\alpha(2\boldsymbol{A}_{12}+\boldsymbol{B}_{12})\boldsymbol{u}_{1}+(2\boldsymbol{A}_{14}+\boldsymbol{B}_{14})(\boldsymbol{u}_{1}\boldsymbol{\partial}+\mathrm{i}\alpha\boldsymbol{w}_{1})+\mathrm{i}[\alpha\boldsymbol{B}_{13}+(\boldsymbol{B}_{14}-\boldsymbol{A}_{14})\boldsymbol{r}^{-1}]\boldsymbol{v}_{1}\},\end{aligned} \tag{A 2}$$

where the elements $\{\boldsymbol{u}_{1},\boldsymbol{v}_{1},\boldsymbol{w}_{1},\boldsymbol{p}_{1}\}$ and $\{\boldsymbol{u}_{1a}^{*},\boldsymbol{v}_{1a}^{*},\boldsymbol{w}_{1a}^{*},\boldsymbol{p}_{1a}^{*}\}$ and the notation $\boldsymbol{r}$ and $\boldsymbol{r}^{-1}$ denotes diagonal matrices with the discretized functions on the diagonal, and $\boldsymbol{\partial}$ represents the differentiation matrix of the first order.

Appendix B. Optimization for the eigenfunction truncated series with indices $|n|\leqslant3$

A more accurate solution for the optimal azimuthally periodic deviations requires an additional coupled set of equations to the sets given in (2.8), such that the series (2.3) is truncated after $|n|=3$. The sets to be solved are then

$$\mathrm{i}\omega\boldsymbol{D}\boldsymbol{a}_{0}=\boldsymbol{M}_{0}\boldsymbol{a}_{0}+\boldsymbol{L}_{0}\boldsymbol{a}_{1},\quad \mathrm{i}\omega\boldsymbol{D}\boldsymbol{a}_{1}=\boldsymbol{M}_{1}\boldsymbol{a}_{1}+\boldsymbol{L}_{1}\boldsymbol{a}_{0}+\boldsymbol{L}_{2}\boldsymbol{a}_{2}, \tag{B 1a, b}$$

$$\mathrm{i}\omega \boldsymbol{D}\boldsymbol{a}_2 = \boldsymbol{M}_2\boldsymbol{a}_2 + \boldsymbol{L}_1\boldsymbol{a}_1 + \boldsymbol{L}_2\boldsymbol{a}_3, \quad \mathrm{i}\omega \boldsymbol{D}\boldsymbol{a}_3 = \boldsymbol{M}_3\boldsymbol{a}_3 + \boldsymbol{L}_1\boldsymbol{a}_2, \tag{B 1c, d}$$

where the matrices $\boldsymbol{L}_1$, $\boldsymbol{L}_2$ and $\boldsymbol{L}_0$ are given by (2.6) and (2.9), respectively. Substituting (B 1*d*) into (B 1*c*) yields a differential relation between $\boldsymbol{a}_2$ and $\boldsymbol{a}_1$, which then can be substituted together with (B 1*a*) into (B 1*b*) to yield a similar equation to (2.10):

$$\mathscr{M}_1\boldsymbol{a}_1 = \boldsymbol{L}_1\mathscr{M}_0^{-1}\boldsymbol{L}_0\boldsymbol{a}_1 + \boldsymbol{L}_2\mathscr{L}_2^{-1}\boldsymbol{L}_1\boldsymbol{a}_1, \tag{B 2}$$

with the modified operator

$$\mathscr{L}_2 = \mathscr{M}_2 - \boldsymbol{L}_2\mathscr{M}_3^{-1}\boldsymbol{L}_1, \tag{B 3}$$

where $\mathscr{M}_2$ and $\mathscr{M}_3$ are given by the definition (2.11).

Equation (B 2) can be used to obtain more accurate eigenmodes for the flow profile which is modified by the optimal deviations computed in § 4.

REFERENCES

Batchelor, G. K. & Gill, A. E. 1962 Analysis of the stability of axisymmetric jets. *J. Fluid Mech.* **14**, 529–551.

Ben-Dov, G. 2006 Optimal disturbances and secondary instabilities in shear flows. PhD thesis, Technion – Israel Institute of Technology, Haifa, Israel.

Ben-Dov, G. & Cohen, J. 2007 Critical Reynolds number for a natural transition to turbulence in pipe flows. *Phys. Rev. Lett.* **98**, 064503.

Ben-Dov, G., Levinski, V. & Cohen, J. 2003 On the mechanism of optimal disturbances: The role of a pair of nearly parallel modes. *Phys. Fluids* **15**, 1961–1972.

Bergström, L. 1993 Optimal growth of small disturbances in pipe Poiseuille flow. *Phys. Fluids* A **5**, 2710–2720.

Biau, D. & Bottaro, A. 2004 Transient growth and minimal defects: Two possible initial paths of transition to turbulence in plane shear flows. *Phys. Fluids* **16**, 3515–3529.

Bottaro, A., Corbett, P. & Luchini, P. 2003 The effect of base flow variation on flow stability. *J. Fluid Mech.* **476**, 293–302.

Butler, K. M. & Farrell, B. F. 1992 Three-dimensional optimal perturbations in viscous shear flow. *Phys. Fluids* A **4** (8), 1637–1650.

Chapman, S. J. 2002 Subcritical transition in channel flows. *J. Fluid Mech.* **451**, 35–97.

Cohen, J. & Wygnanski, I. 1987 The evolution of instabilities in the axisymmetric jet. Part 2. The flow resulting from the interaction between two waves. *J. Fluid Mech.* **176**, 221–235.

Darbyshire, A. G. & Mullin, T. 1995 Transition to turbulence in constant-mass-flux pipe flow. *J. Fluid Mech.* **289**, 83–114.

Davey, A. & Nguyen, H. P. F. 1971 Finite-amplitude stability of pipe flow. *J. Fluid Mech.* **45**, 701–720.

Eckhardt, B., Schneider, T. M., Hof., B. & Westerweel, J. 2007 Turbulence transition in pipe flow. *Annu. Rev. Fluid Mech.* **39**, 447–468.

Eliahou, S., Tumin, A. & Wygnanski, I. 1998 Laminar-turbulent transition in Poiseuille pipe flow subjected to periodic perturbation emanating from the wall. *J. Fluid Mech.* **361**, 333–349.

Elofsson, P. A. & Alfredsson, P. H. 1998 An experimental study of oblique transition in plane Poiseuille flow. *J. Fluid Mech.* **358**, 177–202.

Faisst, H. & Eckhardt, B. 2003 Traveling waves in pipe flow. *Phys. Rev. Lett.* **91**, 2245021-4.

Gavarini, M. I., Bottaro, A. & Nieuwstadt, F. T. M. 2004 The initial stage of transition in pipe flow: role of optimal base-flow distortions. *J. Fluid Mech.* **517**, 131–165.

Gill, A. E. 1965 A mechanism for instability of plane Couette flow and of Poiseuille flow in a pipe. *J. Fluid Mech.* **21**, 503–511.

Gustavsson, L. H. 1991 Energy growth of three-dimensional disturbance in plane Poiseuille flow. *J. Fluid Mech.* **224**, 241–260.

Han, G., Tumin, A. & Wygnanski, I. 2000 Laminar-turbulent transition in Poiseuille pipe flow subjected to periodic perturbation emanating from the wall. Part 2. Late stage of transition. *J. Fluid Mech.* **419**, 1–27.

Henningson, D. S., Lundbladh, A. & Johansson, A. V. 1993 A mechanism for bypass transition from localized disturbances in wall-bounded shear flows. *J. Fluid Mech.* **250**, 169–207.

Hof, B., Doorne, C. W. H. Van, Westerweel, J., Nieuwstadt, F. T. M., Faisst, H., Eckhardt, B., Wedin, H., Kerswell, R. R. & Waleffe, F. 2004 Experimental observations of nonlinear traveling waves in turbulent pipe flow. *Science* **305**, 1594–1598.

Hof, B., Juel, A. & Mullin, T. 2003 Scaling of the turbulent transition threshold in a pipe. *Phys. Rev. Lett.* **91**, 2445021-4.

Itoh, N. 1977 Nonlinear stability of parallel flows with subcritical Reynolds numbers. Part 2. Stability of pipe Poiseuille flow to finite axisymmetric disturbances. *J. Fluid Mech.* **82**, 469–479.

Kerswell, R. R. 2005 Recent progress in understanding the transition to turbulence in a pipe. *Nonlinearity* **18**, R17–R44.

Lerner, J. & Knobloch, E. 1988 The long-wave instability of a defect in a uniform parallel shear. *J. Fluid Mech.* **189**, 117–134.

Lessen, M., Sadler, G. S. & Liu, T. 1968 Stability of pipe Poiseuille flow. *Phys. Fluids* **11**, 1404–1409.

Meseguer, A. 2003 Streak breakdown instability in pipe Poiseuille flow. *Phys. Fluids* **15**, 1203–1213.

Meseguer, A. & Trefethen, L. N. 2003 Linearized pipe flow to Reynolds number 10^7. *J. Comput. Phys.* **186**, 178–197.

Orszag, S. A. & Patera, A. T. 1983 Secondary instability of wall-bounded shear flows. *J. Fluid Mech.* **128**, 347–385.

Patel, V. C. & Head, M. R. 1969 Some observations on skin friction and velocity profiles in fully developed pipe and channel flows. *J. Fluid Mech.* **38**, 181–201.

Peixinho, J. & Mullin, T. 2006 Decay of turbulence in pipe flow. *Phys. Rev. Lett.* **96**, 094501-4.

Pfeniger, W. 1961 Boundary layer suction experiments with laminar flow at high Reynolds numbers in the inlet length of a tube by various suction methods. In *"Boundary Layer and Flow Control* (ed. G. V. Lachman), pp. 961–980. Pergamon.

Philip, J., Svizher, A. & Cohen, J. 2007 Scaling law for subcritical transition in plane Poiseuille flow. *Phys. Rev. Lett.* **98**, 154502.

Reddy, S. C. & Henningson, D. S. 1993 Energy growth in viscous channel flows. *J. Fluid Mech.* **252**, 209–238.

Reshotko, E. 2001 Transient growth: A factor in bypass transition. *Phys. Fluids* **13**, 1067–1075.

Reshotko, E. & Tumin, A. 2001 Spatial theory of optimal disturbances in a circular pipe flow. *Phys. Fluids* **13**, 991–996.

Reynolds, O. 1883 An experimental investigation of the circumtances which determine whether motion of water shall be direct or sinous and of the law of resistance in parallel channels. *Phil. Trans. R. Soc. Lond.* **174**, 935–982.

Romanov, V. A. 1973 Stability of plane-parallel Couette flow. *Funct. Anal. Appl.* **7** (2), 137–146.

Rubin, Y., Wygnanski, I. & Haritonidis, J. H. 1980 Further observations on transition in a pipe. In *Laminar-Turbulent Transition* (ed. R. Eppler & H. Fasel), pp. 19–26. Springer.

Salwen, H., Cotton, F. W. & Grosch, C. E. 1980 Linear stability of Poiseuille flow in a circular pipe. *J. Fluid Mech.* **98**, 273–284.

Schmid, P. J. & Henningson, D. S. 1994 Optimal energy density growth in Hagen-Poiseuille flow. *J. Fluid Mech.* **277**, 197–225.

Schmid, P. J. & Henningson, D. S. 2001 *Stability and Transition in Shear Flows*. Springer.

Schneider, T. M., Eckhardt, B. & Yorke, J. A. 2007 Turbulence transition and the edge of chaos in pipe flow. *Phys. Rev. Lett.* (to appear).

Smith, F. T. & Bodonyi, R. J. 1982 Amplitude-dependent neutral modes in Hagen-Poiseuille flow through a circular pipe. *Proc. R. Soc. Lond.* A **384**, 463–489.

Svizher, A. & Cohen, J. 2006 Holographic particle image velocimetry measurements of hairpin vortices in a subcritical air channel flow. *Phys. Fluids* **18**, 014105-1-14.

Thomas, L. H. 1953 The stability of plane-Poiseuille flow. *Phys. Rev.* **91**, 780–783.

Tillmark, N. & Alfredsson, H. 1992 Experiments on transition in plane Couette flow. *J. Fluid Mech.* **235**, 89–102.

Waleffe, F. 1995 Hydrodynamic stability and turbulence: beyond transients to a self-sustaining process. *Stud. Appl. Maths.* **95**, 319–343.

Waleffe, F. 1997 On a self-sustaining process in shear flows. *Phys. Fluids* **9**, 883–900.

Wedin, H. & Kerswell, R. R. 2004 Exact coherent structures in pipe flow: travelling wave solutions. *J. Fluid Mech.* **508**, 333–371.

Willis, A. P. & Kerswell, R. R. 2007 Critical behavior in the relaminarization of localized turbulence in pipe flow. *Phys. Rev. Lett.* **98**, 014501-4.

Wygnanski, I. J. & Champagne, F. H. 1973 On transition in a pipe. Part 1. The origin of puffs and slugs and the flow in a turbulent slug. *J. Fluid Mech.* **59**, 281–335.

Wygnanski, I., Sokolov, M. & Friedman, D. 1975 On transition in a pipe. Part 2. The equilibrium puff. *J. Fluid Mech.* **69**, 283–304.

Zikanov, O. Y. 1996 On the stability of pipe Poiseuille flow. *Phys. Fluids* **8** (11), 2923–2932.